Monthly Notices of the ROYAL ASTRONOMICAL SOCIETY

MNRAS **527,** 6950–6969 (2024) https://doi.org/10.1093/mnras/stad3559
Advance Access publication 2023 November 20

The DESI One-Percent Survey: exploring a generalized SHAM for multiple tracers with the UNIT simulation

Jiaxi Yu,[1★] Cheng Zhao,[1,2★] Violeta Gonzalez-Perez,[3,4] Chia-Hsun Chuang,[5] Allyson Brodzeller,[5] Arnaud de Mattia,[6] Jean-Paul Kneib,[1,7] Alex Krolewski,[8,9,10] Antoine Rocher,[6] Ashley Ross,[11] Yunchong Wang,[13] Sihan Yuan,[12,14] Hanyu Zhang,[15] Rongpu Zhou,[16] Jessica Nicole Aguilar,[16] Steven Ahlen,[17] David Brooks,[18] Kyle Dawson,[5] Alex de la Macorra,[19] Peter Doel,[18] Kevin Fanning,[11,20] Andreu Font-Ribera,[21] Jaime Forero-Romero,[22] Satya Gontcho A Gontcho,[16] Klaus Honscheid,[11,20] Robert Kehoe,[23] Theodore Kisner,[16] Anthony Kremin,[16] Martin Landriau,[16] Marc Manera,[21,24] Paul Martini,[11,25] Aaron Meisner,[26] Ramon Miquel,[21,27] John Moustakas,[28] Jundan Nie,[29] Will Percival,[8,9,10] Claire Poppett,[16,30,31] Anand Raichoor,[16] Graziano Rossi,[32] Hee-Jong Seo,[33] Gregory Tarlé,[34] Zhimin Zhou[29] and Hu Zou[29]

Affiliations are listed at the end of the paper

Accepted 2023 November 14. Received 2023 November 14; in original form 2023 June 15

ABSTRACT

We perform SubHalo Abundance Matching (SHAM) studies on UNIT simulations with $\{\sigma, V_{\rm ceil}, v_{\rm smear}\}$-SHAM and $\{\sigma, V_{\rm ceil}, f_{\rm sat}\}$-SHAM. They are designed to reproduce the clustering on 5–30 h^{-1} Mpc of luminous red galaxies (LRGs), emission-line galaxies (ELGs), and quasi-stellar objects (QSOs) at $0.4 < z < 3.5$ from DESI (Dark Energy Spectroscopic Instrument) One Percent Survey. $V_{\rm ceil}$ is the incompleteness of the massive host (sub)haloes and is the key to the generalized SHAM. $v_{\rm smear}$ models the clustering effect of redshift uncertainties, providing measurements consistent with those from repeat observations. A free satellite fraction $f_{\rm sat}$ is necessary to reproduce the clustering of ELGs. We find ELGs present a more complex galaxy–halo mass relation than LRGs reflected in their weak constraints on σ. LRGs, QSOs, and ELGs show increasing $V_{\rm ceil}$ values, corresponding to the massive galaxy incompleteness of LRGs, the quenched star formation of ELGs and the quenched black hole accretion of QSOs. For LRGs, a Gaussian $v_{\rm smear}$ presents a better profile for subsamples at redshift bins than a Lorentzian profile used for other tracers. The impact of the statistical redshift uncertainty on ELG clustering is negligible. The best-fitting satellite fraction for DESI ELGs is around 4 per cent, lower than previous estimations for ELGs. The mean halo mass $\log_{10}(\langle M_{\rm vir}\rangle)$ in $h^{-1}\,{\rm M}_{\odot}$ for LRGs, ELGs, and QSOs are 13.16 ± 0.01, 11.90 ± 0.06, and 12.66 ± 0.45, respectively. Our generalized SHAM algorithms facilitate the production of multitracer galaxy mocks for cosmological tests.

Key words: methods: observational – methods: statistical – Galaxy: halo – large-scale structure of Universe.

1 INTRODUCTION

Lambda-cold dark matter is the standard model of modern cosmology that describes the evolution of the universe. In this framework, two dark components, dark matter, and dark energy, comprise 95 per cent of the total energy density. The nature of dark energy can be explored using baryonic acoustic oscillation (BAO; Eisenstein & Hu 1998), a standard ruler of the universe. Meanwhile, redshift-space distortion (RSD, Kaiser 1987) embodies the growth rate of the large-scale structure (LSS) which is dominated by the evolution of dark matter.

In observation, BAO and RSD can be measured by spectroscopic galaxy surveys that observe millions of spectra of galaxies and quasi-stellar objects (QSOs). With BAO and RSD, the precision of cosmological parameters, such as Ω_Λ, H_0, and σ_8, have reached per cent level (Alam et al. 2021b), constrained with data from the Baryon Oscillation Spectroscopic Survey (BOSS, 2008–2014; Dawson et al. 2012), and the extended BOSS (eBOSS, 2014–2020; Dawson et al. 2016) in the Sloan Sky Digital Survey[1] (SDSS; Eisenstein et al. 2011; Blanton et al. 2017). BOSS and eBOSS have probed 1 547 553 luminous red galaxies (LRGs) at $0.2 < z < 1.0$, 173 736 emission-line galaxies (ELGs) at $0.6 < z < 1.1$, and 343 708 QSOs at $0.8 < z < 2.2$ (Alam et al. 2021a).

The largest ongoing spectroscopic survey, the Dark Energy Spectroscopic Instrument (DESI, 2021–2026; DESI Collaboration 2016a,b) is a robotic, fibre-fed, highly multiplexed survey that operates on the Mayall 4-m telescope at Kitt Peak National Observatory.

★ E-mail: jiaxi.yu@epfl.ch (JY); czhao@tsinghua.edu.cn (CZ)

[1] http://www.sdss.org/

© 2023 The Author(s)
Published by Oxford University Press on behalf of Royal Astronomical Society. This is an Open Access article distributed under the terms of the Creative Commons Attribution License (https://creativecommons.org/licenses/by/4.0/), which permits unrestricted reuse, distribution, and reproduction in any medium, provided the original work is properly cited.

Downloaded from https://academic.oup.com/mnras/article/527/3/6950/7438901 by University College London user on 06 February 2024

It aims to explore the nature of dark energy via the most precise measurement of the 3D universe in 14 000 $\deg^2$ of the sky after 5 yr of observations (Levi et al. 2013). The list of targets to be observed by DESI (Myers et al. 2023) is determined with the help of the imaging from the DESI Legacy Imaging Surveys (Zou et al. 2017; Dey et al. 2019; Schlegel et al. in preparation). The preliminary selection of targets was done in 2020 for the Milky Way Survey (Allende Prieto et al. 2020), Bright Galaxy Survey (BGS; Ruiz-Macias et al. 2020), LRG (Zhou et al. 2020), ELG (Raichoor et al. 2020), and QSO (Yèche et al. 2020).

DESI started its first light observation in 2020 and will make public its early data release (EDR, DESI Collaboration 2023a) and the Siena Galaxy Atlas (Moustakas et al. in preparation) in 2023. EDR contains LSS catalogues that include redshift measurements, their corresponding random catalogues, and the clustering output (DESI Collaboration 2023b; Lasker et al. in preparation). The One Percent Survey is a part of the EDR. It has covered around one per cent of the 5-yr sky footprint and observed more than 90 000 LRGs, 270 000 ELGs, 30 000 QSOs, and 150 000 low-redshift galaxies in BGS (DESI Collaboration 2023a). Despite the smaller numbers of galaxies and QSOs compared to the SDSS data, the number densities of tracers from the DESI One Percent Survey are larger than those of BOSS and eBOSS (introduced later in Table 2). Additionally, the rate between the observed targets and the targets of the One Percent Surveys is larger than 85 per cent for all tracers (DESI Collaboration 2023b; Lasker et al. in preparation). Thus, data from the One Percent Survey are sufficient for small-scale clustering analysis, such as the galaxy–halo connection study.

The relationship between haloes and galaxies is crucial for the modelling of galaxy clustering. However, this relation is highly non-linear and generally subject to local environmental effects (e.g. Tinker, Wetzel & Conroy 2011; Wetzel, Tinker & Conroy 2012). SubHalo Abundance Matching (SHAM, Kravtsov et al. 2004; Tasitsiomi et al. 2004; Conroy, Wechsler & Kravtsov 2006; Behroozi, Conroy & Wechsler 2010) is an intuitive empirical method to model this non-linear relation based on N-body simulations that resolve hierarchical structures, including both haloes and subhaloes. This method assigns the most massive or brightest galaxy to centres of the most massive haloes in the case of central galaxies and subhaloes for satellite galaxies. The resulting probability of hosting a central/satellite galaxy in a halo/subhalo is a function of their (sub)halo mass, $P(M_{\rm halo})$. The shape of this probability is related to the stellar properties determined empirically.

As clustering observations and simulations improve, more advanced versions of SHAM algorithms are developed. For instance, Tasitsiomi et al. (2004) introduced a Gaussian scattering with dispersion σ to the halo mass, to model the Gaussian residual in the galaxy–halo mass relation (e.g. Willick et al. 1997; Steinmetz & Navarro 1999). Trujillo-Gomez et al. (2011) and Reddick et al. (2013) proposed using the peak maximum circular velocity, $V_{\rm peak}$, instead of the halo mass, $M_{\rm vir}$, as it is closely associated with stellar mass and it is immune to the tidal stripping of subhaloes and pseudo-evolution of their $M_{\rm vir}$. Favole et al. (2016) and Rodríguez-Torres et al. (2017) proposed a SHAM implementation that takes into account the fact that ELGs and QSOs are incomplete in the massive stellar-mass end. There are also SHAM variants that make use of secondary halo/galaxy properties (e.g. Hearin et al. 2013; Favole et al. 2022). SHAM methods can also include assembly bias and orphan galaxies (Lehmann et al. 2017; Behroozi et al. 2019; Contreras, Angulo & Zennaro 2021b; DeRose, Becker & Wechsler 2022).

In this work, we use two SHAM implementations that are essentially variants of one algorithm: $\{\sigma, V_{\rm ceil}, v_{\rm smear}\}$-SHAM ($v_{\rm smear}$-SHAM hereafter) and $\{\sigma, V_{\rm ceil}, f_{\rm sat}\}$-SHAM ($f_{\rm sat}$-SHAM hereafter). The $v_{\rm smear}$-SHAM was used to study BOSS/eBOSS LRGs (Yu et al. 2022, Yu22 hereafter) and here we use it to model LRGs and QSOs. Here, we introduce the $f_{\rm sat}$-SHAM to be able to correctly reproduce the clustering of DESI ELGs. The free parameters in these SHAMs model the following aspects: the scatter in the galaxy–halo mass relation, σ; an upper limit of σ-scattered $V_{\rm peak}$ set by $V_{\rm ceil}$ (in percentage), which reduces the possibility of massive (sub)haloes hosting a given type of galaxy or QSO; the uncertainty in spectroscopic redshift determination, $v_{\rm smear}$; and the fraction of satellite galaxies, $f_{\rm sat}$, which we find to be only needed for reproducing the clustering of ELGs.

This paper is arranged as follows. In Section 2, we describe the EDR of DESI, including repeat observations and statistical redshift uncertainty measurements, the UNIT (Universe N-body simulations for the Investigation of Theoretical models) N-body simulation, and the covariance matrix. The SHAM implementation and fitting are introduced in Section 3. In Section 4, we present the best-fitting results of SHAM and the interpretations of parameters for different tracers. We conclude our findings in Section 5.

This paper is one of the first series papers from the DESI galaxy–halo connection topical group. Papers released with EDR for One Percent Survey analysis that utilize ABACUSSUMMIT (Maksimova et al. 2021) simulations are Yuan et al. (2023a) for LRG and QSO HOD (halo occupation distribution), and Rocher et al. (2023) for ELG HOD. Prada et al. (2023) is an overview for SHAM based on UCHUU (Ishiyama et al. 2021). A stellar-mass-split abundance matching applied on COSMICGROWTH (Jing 2019) is also used to study DESI LRG–ELG cross-correlations (Gao et al. 2023, Yuan et al. 2023b). Other works will be published along with later data releases.

2 DATA

2.1 DESI early data release

DESI, a 5-yr spectroscopic survey, started instrumental tests in 2020 to ensure the 5000 fibres controlled by the robotic positioners could work properly in the focal plane over a 3° field of view (DESI Collaboration 2022; Silber et al. 2022; Miller et al. 2023). After the commissioning, DESI conducted its Survey Validation campaign (DESI Collaboration 2023a). It aims to validate the spectra reduction pipeline (Guy et al. 2023), assess the quality of data provided by REDROCK[2] that derives the target type and redshift from spectra (Bailey et al. in preparation), and optimize the target selection (Schlafly et al. 2023) and fibre assignment (Raichoor et al. in preparation) of DESI. During the campaign, it explores target selection criteria broader than those of the 5-yr main survey and observes objects typically four times longer than the main survey; in addition, to perform the visual inspection, few tiles are observed approximately 10 times longer than in the main survey (Alexander et al. 2023; Lan et al. 2023). For this reason, there are many repeat observations for each object. Later in 2021 April and May, DESI observed its One Percent Survey that covered about 1 per cent of the footprint of the 5-yr main survey and used target selection criteria close to those of the main survey (Chaussidon et al. 2023; Cooper et al. 2023; Hahn et al. 2023; Raichoor et al. 2023; Zhou et al. 2023). The observation field is composed of 20 non-overlapping rosettes, each observed at least 12 times. This ensures very high fibre assignment completeness (larger than 85 per cent for ELGs and over 94 per cent for the rest of the tracers) in this region (DESI Collaboration 2023a,b; Lasker et al. in preparation). As there are

[2]https://github.com/desihub/redrock

Downloaded from https://academic.oup.com/mnras/article/527/3/6950/7438901 by University College London user on 06 February 2024

more exposures for objects that do not have a reliable redshift after the first observation, data from the One Percent Survey have a high redshift-success rate.

Our SHAM method aims to reproduce the clustering of LRGs at $0.4 < z < 1.1$, ELGs at $0.8 < z < 1.6$, and QSOs at $0.8 < z < 3.5$ from the One Percent Survey in the range 5–30 h^{-1} Mpc. LRG samples are divided into three smaller redshift ranges: $0.4 < z < 0.6$, $0.6 < z < 0.8$, $0.8 < z < 1.1$. ELG samples are divided into two redshift bins: $0.8 < z < 1.1$ and $1.1 < z < 1.6$. QSOs are observed at $0.8 < z < 3.5$, and are divided into $0.8 < z < 1.1$, $1.1 < z < 1.6$, $1.6 < z < 2.1$, and $2.1 < z < 3.5$.

2.1.1 *Galaxy weights*

To obtain an unbiased measurement in the galaxy clustering, we employ the FKP weight $w_{\rm FKP}$, the pairwise-inverse-probability (PIP) weight (Bianchi & Percival 2017), and the angular-up weight (ANG, Percival & Bianchi 2017) for pairs of galaxies. In the calculation of the effective redshift, we use the total weight $w_{\rm tot}$

$$w_{\rm tot} = w_{\rm FKP} w_{\rm comp}. \tag{1}$$

where $w_{\rm comp}$ is the fibre-assignment completeness weight provided in the LSS catalogue. We briefly describe all of them below and we refer the readers to DESI Collaboration (2023b) and Lasker et al. (in preparation) for more details.

The One Percent Survey LSS catalogues provide $w_{\rm FKP}$ (Feldman, Kaiser & Peacock 1994) that minimizes the variance in the clustering estimator (see Section 3.1) when the observed number density of tracers varies with redshift

$$w_{\rm FKP} = \frac{1}{1 + \bar{n}(z) P_0}, \tag{2}$$

where $\overline{n}(z)$ is the average number density at redshift z, and P_0 is the amplitude of the observed power spectrum at $k \approx 0.15\,h\,{\rm Mpc}^{-1}$. $P_0 = 10000, 4000, 6000\,h^{-3}\,{\rm Mpc}^3$ for LRGs, ELGs and QSOs respectively (DESI Collaboration 2023b).

The PIP+ANG weighting scheme has been developed to correct the missing galaxy pairs due to fibre collision. Mohammad et al. (2020) have proved that PIP+ANG weights provide an unbiased clustering down to 0.1 h^{-1} Mpc. So the clustering measurement provided by the EDR has implemented this weighting scheme in addition to $w_{\rm FKP}$ (Section 3.1). The $w_{\rm comp}$ provided in the LSS catalogues is for correcting the observational incompleteness due to the fibre assignment (DESI Collaboration 2023b). PIP and ANG weights, as well as $w_{\rm comp}$, are all calculated with simulations of fibre assignment as described in Lasker et al. (in preparation).

We calculate the effective redshift of pairs of galaxies at redshifts z_i and z_j (e.g. Bautista et al. 2021), with

$$z_{\rm eff} = \frac{\sum_{i,j} w_{{\rm tot},i} w_{{\rm tot},j} (z_i + z_j)/2}{\sum_{i,j} w_{{\rm tot},i} w_{{\rm tot},j}}, \tag{3}$$

The effective volume $V_{\rm eff,\,obs}$ (Wang, Chuang & Hirata 2013) also involves P_0 as

$$V_{\rm eff} = \sum_i \left(\frac{\bar{n}(z_i) P_0}{1 + \bar{n}(z_i) P_0} \right)^2 \Delta V(z_i), \tag{4}$$

where $\Delta V(z_i)$ is the comoving survey volume and $\overline{n}(z_i)$ is the mean number density of the tracer inside the redshift bin z_i. The effective number density is calculated as

$$n_{\rm eff} = \sqrt{\frac{\sum_i \bar{n}(z_i)^2 \Delta V(z_i)}{\sum_i \Delta V(z_i)}}. \tag{5}$$

We present in Table 2 all the tracers we use, their redshift ranges and the corresponding effective redshifts $z_{\rm eff}$, the effective volume $V_{\rm eff}$, and the number density $n_{\rm eff}$.

2.2 Repeat observations and statistical redshift uncertainty

The spectroscopic measurements of redshift have associated uncertainties (i.e. the redshift uncertainty) due to factors like the spectral line width, observing conditions, and different astrophysical effects. The impact of the redshift uncertainty is equivalent to adding stochasticity to the peculiar velocity of the observed object, and thus will bias the measurement of anisotropic clustering and velocity bias (Guo et al. 2015; Hou et al. 2018; Yu et al. 2022). The redshift uncertainty can be quantified by repeat observations statistically and via its influence on the clustering using our SHAM method (see Section 3.2). The results of those two estimators should be consistent.

Objects observed repetitively exist in all stages of Survey Validation. However, the ones from the One Percent Survey are biased towards faint objects by design (see Section 2.1). Therefore, we used data from the early stage of Survey Validation to obtain an unbiased estimate of the redshift uncertainty. The redshift difference, Δz, is calculated for all pairs of repeated spectra for each object and then converted to radial velocity using $\Delta v = c\Delta z/(1 + z)$, where c is the speed of light and z is the mean redshift of the pairs. Δv measurements larger than the redshift failure threshold (1000 km s^{-1} for LRGs and ELGs and 3000 km s^{-1} for QSOs) are then removed.

The histograms of the redshift difference of ELGs, LRGs, and QSOs are presented in Fig. 1 in black dots. The error bars of those histograms are calculated using the delete-one jackknife method. Our fitting range is around $[-200, 200]$ km s^{-1} for LRGs, $[-150, 150]$ km s^{-1} for ELGs, and $[-1600, 1600]$ km s^{-1} for QSOs except for $[-500, 500]$ km s^{-1} for QSOs at $0.8 < z < 1.1$. The title of each subplot in Fig. 1 shows the percentage of Δv measurements that are beyond the fitting range. For SDSS BOSS/eBOSS LRGs, the redshift difference in all redshift ranges can be well fitted by Gaussian functions (Lyke et al. 2020; Ross et al. 2020; Yu et al. 2022). For DESI, all tracers show a preference for Lorentzian distributions in general (solid lines in Fig. 1) as

$$\mathcal{L}(p, w_{\Delta v}) = \frac{A}{1 + ((x - p)/w_{\Delta v})^2}. \tag{6}$$

In equation (6), A is a normalization factor, p is the location of the peak value on the x-axis, and $2w_{\Delta v}$ is the full-width at half maximum of the Lorentzian distribution. In addition, we also try to describe Δv histograms of LRGs with Gaussian profiles $\mathcal{N}(\mu, \sigma_{\Delta v})$ (dashed lines in Fig. 1). We will discuss which profile to use for SHAM in Section 4.4. As p and μ are well consistent with 0, we only present the best-fitting Lorentzian $w_{\Delta v}$ and Gaussian $\sigma_{\Delta v}$ on the labels of Fig. 1. We also calculate the standard deviation of the redshift difference $\hat{\sigma}_{\Delta v}$.

In Fig. 1, we observe a much smaller redshift uncertainty for the ELGs than that of the LRGs and QSOs. The maximum $w_{\Delta v}$ of ELGs is 13.4 ± 0.1 km s^{-1}, while the minimum $w_{\Delta v}$ of LRG and QSOs is 34.6 ± 0.9 and 30.2 ± 0.2 km s^{-1}, respectively. This can be attributed to the narrow [O II] emission for ELG redshift determination, compared with absorption lines of LRGs and broad emissions of QSOs. Additionally, galaxy samples (LRGs and ELGs) show increasing uncertainty with redshift. This is because galaxies are fainter at higher redshift, and spectral lines for redshift determination have a decreasing signal-to-noise ratio and larger uncertainty. But for QSO this is not the case, as QSOs at higher redshifts are not necessarily fainter. Another reason for the non-monotonic QSO $w_{\Delta v}$ trend is that

Downloaded from https://academic.oup.com/mnras/article/527/3/6950/7438901 by University College London user on 06 February 2024

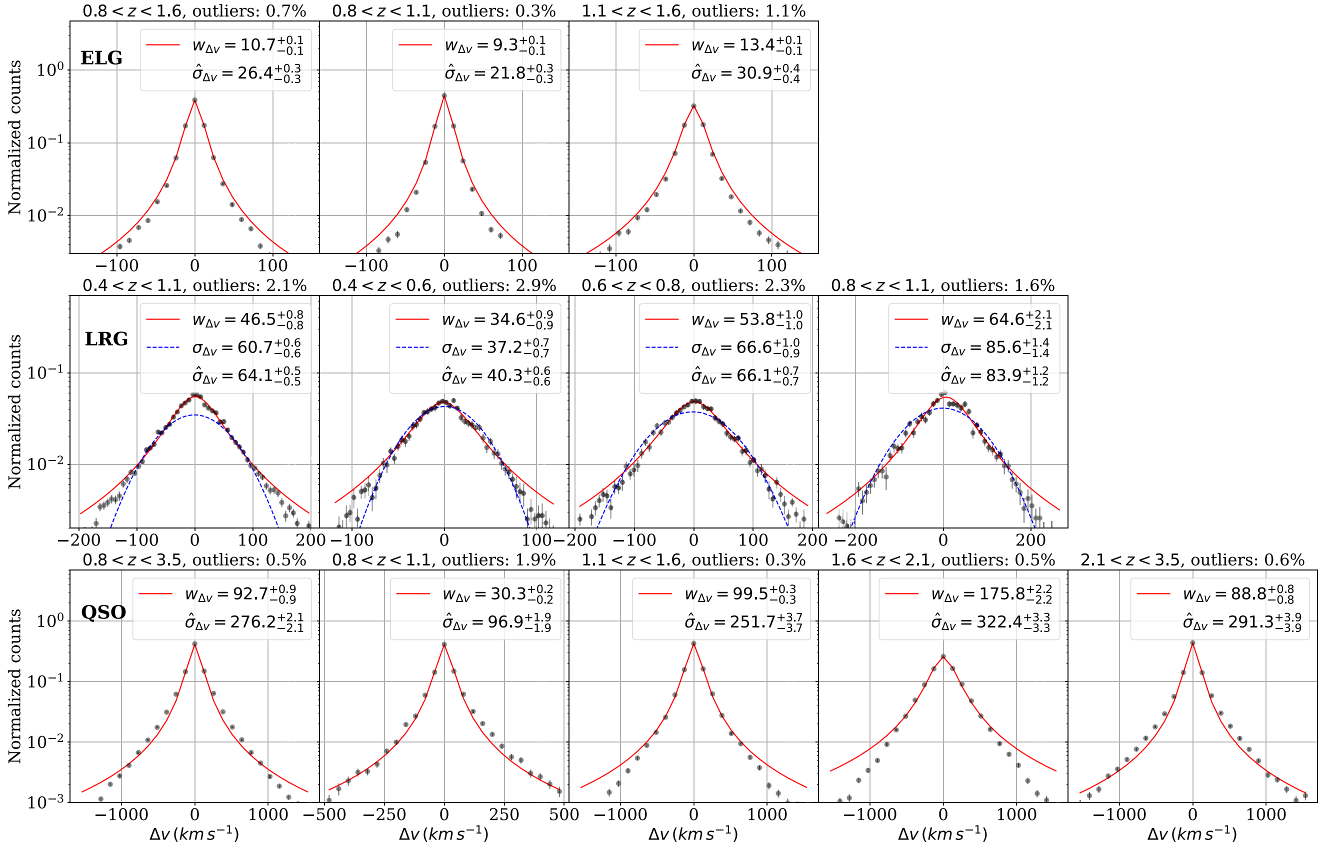

Figure 1. The statistical redshift uncertainty estimated with the histogram of the redshift difference (filled circles with error bars) from repeat observation taken during the early stage of Survey Validation. The first, second, and third rows are ELGs, LRGs, and QSOs, respectively. The first columns of all rows are results for total samples, while the rest are for subsamples at redshift bins. The statistical redshift uncertainty measured by Lorentzian functions $w_{\Delta v}$ (solid lines) and standard deviations $\hat{\sigma}_{\Delta v}$ of Δv is presented in the label of each subplot. For LRG samples, we also fit Δv histograms with Gaussian functions (dashed lines), providing their best-fitting dispersion $\sigma_{\Delta v}$ in the label as well. The fraction of Δv that are not included in the fittings is indicated as outlier fractions in titles.

the measurement made by repeat observation is no longer reliable at $z \gtrsim 1.5$. We will explain this in detail in Section 4.4.

2.3 *N*-body simulation: UNIT

We apply our SHAM on UNIT models from galaxy surveys[3] (Chuang et al. 2019) to generate model galaxies in cubic boxes. *Planck* cosmology (Planck Collaboration XIII 2016) is employed in the UNIT simulations and our SHAM implementation: $\Omega_{\rm m} = 0.3089$, $h \equiv H_0/100\,{\rm km\,s^{-1}\,Mpc^{-1}} = 0.6774$, $n_s = 0.9667$, and $\sigma_8 = 0.8147$. In each 1 $h^{-3}\,{\rm Gpc}^3$ UNIT simulation box, there are 4096^3 particles with the mass resolution of $1.2 \times 10^9\ h^{-1}\,{\rm M}_\odot$.

We use UNIT halo catalogues with subhaloes identified by the ROCKSTAR (Behroozi, Wechsler & Wu 2013a) halo finder that provides properties at the current snapshot, such as positions, peculiar velocities, virial mass $M_{\rm vir}$, and the maximum circular velocity $V_{\rm max}$. We regard $M_{\rm vir}$ of haloes with more than 50 dark matter particles to be reliable, that is, $M_{\rm vir}^{\rm good} > 6 \times 10^{10}\,h^{-1}\,{\rm M}_\odot$. The merger/stripping histories of haloes and subhaloes are provided by CONSISTENT TREES (Behroozi et al. 2013b). They are used to determine their peak maximum circular velocity throughout the accretion history, tha is, $V_{\rm peak}$, which is the proxy of halo mass in our SHAM study.

UNIT simulations are created using the fixed-amplitude method implemented in pairs of simulation boxes to suppress the cosmic variance (Angulo & Pontzen 2016; Chuang et al. 2019). The effective volume of UNIT simulations is much larger than those of DESI EDR tracers as shown in Table 2. So we can take just one simulation box in each snapshot and ignore the influence of the UNIT cosmic variance on our SHAM fitting.

UNIT includes 128 snapshots of simulations from redshift 99 to 0 and we employ 14 of them with their redshift presented in the fourth column of Table 2. We select the UNIT snapshot whose redshift is the closest to the $z_{\rm eff}$ (equation 3) of the corresponding DESI sample among all the snapshots.

3 METHOD

3.1 Galaxy clustering

The two-point correlation function (2PCF) measures the excess probability of finding a galaxy pair compared to a random distribution in a given volume. For observations, we use the Landy–Szalay estimator (LS; Landy & Szalay 1993) which minimizes the variances of the measurements for an irregular geometry:

$$\xi_{\rm LS} = \frac{\rm DD - 2DR + RR}{\rm RR}, \tag{7}$$

[3] http://www.unitsims.org/

Downloaded from https://academic.oup.com/mnras/article/527/3/6950/7438901 by University College London user on 06 February 2024

where the data–data (DD), data–random (DR), and random–random (RR) pair counts are normalized by their corresponding total number of pairs. ξ and the pair counts can be calculated as a function of the pair separation s and μ which is the cosine of the angle between the line connecting the galaxy pairs and the line of sight. $w_{\rm FKP}$ is applied to every individual galaxy in the data and random catalogue. PIP weights are applied to DD pair counts, and ANG weights are implemented to both the DD and DR pairs.

The SHAM galaxies are populated in periodic boxes based on halo catalogues from the UNIT *N*-body simulation, so we use the Peebles–Hauser estimator (PH; Peebles & Hauser 1974) to obtain their 2PCF as follows:

$$\xi_{\rm PH} = \frac{\rm DD}{\rm RR} - 1. \tag{8}$$

Unlike observation that requires random catalogues to calculate RR pairs, we use the following expression to calculate them analytically in the simulation box:

$$\mathrm{RR} = \frac{4\pi}{3}\frac{s_{\rm max}^3 - s_{\rm min}^3}{V_{\rm box}}\frac{1}{N_\mu}, \tag{9}$$

where $s_{\rm max}$ and $s_{\rm min}$ are the boundaries of the separation bins, $V_{\rm box} = 1\,h^{-3}\,\mathrm{Gpc}^3$ is the volume of the UNIT simulation box, and $N_\mu = 200$ is the number of μ bins.

By weighting the 2D $\xi(s, \mu)$ with Legendre polynomials $P_\ell(\mu)$, we obtain the 1D ξ multipoles as

$$\xi_\ell(s) = \frac{2\ell+1}{2}\int_{-1}^{1}\xi(s,\mu)P_\ell(\mu)\mathrm{d}\mu. \tag{10}$$

We fit our SHAM to observations based on the monopole and quadrupole, that is, $\ell = 0, 2$. We use 10 logarithmic s bins in $(5, 30)\,h^{-1}$ Mpc and 200 μ bins in $(-1, 1)$.

The projected 2PCF is calculated for cross-checking the clustering of the best-fitting SHAM galaxies. This is calculated as

$$w_p(r_p) = \int_{-\pi_{\rm max}}^{\pi_{\rm max}}\xi(r_p,\pi)\mathrm{d}\pi, \tag{11}$$

where $\pi_{\rm max} = 30\,h^{-1}$ Mpc to avoid the contamination of the systematics on larger scales as shown in Yu22. PYCORR and CORRFUNC PYTHON packages (Sinha & Garrison 2019; Sinha & Garrison 2020) are used to calculate $\xi_\ell(s)$ and w_p.

In observations, 2PCFs are calculated in redshift space. So the position of our mock galaxies produced by SHAM should take into account the RSD (Kaiser 1987) using:

$$Z_{\rm redshift} = Z_{\rm real} + \frac{v_{\rm pec,Z}(1+z)}{H(z)}, \tag{12}$$

where *Z* is the coordinate in the *Z*-axis which is the line of sight, and its subscripts 'redshift' and 'real' illustrate that the coordinate is in the redshift space or in the real space. $v_{\rm pec,\,Z}$ is the proper peculiar velocity of SHAM galaxies along the *Z*-axis, and z is the redshift of the simulation snapshot. As the cosmic variance of UNIT simulations is small, we can safely ignore the variations in quadrupoles for different line of sights (Smith et al. 2021).

3.2 SHAM implementation

SHAM is an empirical method to construct a realistic, monotonic galaxy–halo mass relation based on *N*-body simulations. In its simplest form, a SHAM has a single free parameter σ relating the masses of galaxies and haloes and can successfully reproduce the observed clustering (e.g. Tasitsiomi et al. 2004; Behroozi et al. 2010). As observations provide the clustering of multiple tracers with higher and higher accuracy, this prototype should also be improved. We thus introduce the massive (sub)halo incompleteness $V_{\rm ceil}$, the redshift uncertainty $v_{\rm smear}$, and a free satellite fraction $f_{\rm sat}$ in the SHAM implementation besides the galaxy–halo mass scatter σ. Their impact on the 2PCF $\xi_\ell(s)$ and projected 2PCF $w_p(r_p)$ are presented in Appendix A.

In our study, all (sub)haloes in the simulation have their $V_{\rm peak}$ multiplied by an asymmetric Gaussian as

$$V_{\rm scat} = V_{\rm peak} \times \begin{cases} 1 + \mathcal{N}(0,\sigma), & \mathcal{N}(0,\sigma) > 0; \\ \exp(\mathcal{N}(0,\sigma)), & \mathcal{N}(0,\sigma) < 0, \end{cases} \tag{13}$$

to avoid negative $V_{\rm scat}$.

Then those (sub)haloes are sorted in descending order of $V_{\rm scat}$ and the first $V_{\rm ceil}N_{\rm UNIT}/100$ ones are removed. $N_{\rm UNIT}$ is the total number of haloes and subhaloes in this UNIT simulation. It means the most massive (sub)haloes will not be assigned with a galaxy/QSO in its centre. $V_{\rm ceil}$ is introduced for target selections that possibly remove some of the most massive LRGs, resulting in incompleteness in the host (sub)halo mass. ELGs are mostly star-forming galaxies and thus are not expected to be complete in stellar mass and thus (sub)halo mass (e.g Gonzalez-Perez et al. 2020; Hadzhiyska et al. 2021). This is because the hot and dense centre of massive (sub)haloes is an environment that depletes the cold gas and thus stops star formation (e.g. Kauffmann et al. 2004; Dekel & Birnboim 2006; Peng et al. 2010). QSOs are bright active galactic nuclei (AGNs), that is,their supermassive black holes actively accrete cold gas via discs (e.g. Rosario et al. 2013). In the semi-analytical models (SAM), the formation of AGNs with $L_{\rm bol} \gtrsim 10^{45.1}$ erg s^{-1} only happens at haloes with $M_{\rm vir} \lesssim 10^{13}\ h^{-1}\,\mathrm{M}_\odot$ during starbursts (Griffin et al. 2019). Uchiyama et al. (2018) attribute the absence of QSOs in the overdense regions (i.e. massive haloes) at $z \sim 2$–3 to the lack of wet mergers which leads to the QSO activity. In hydrodynamical simulations, Weinberger et al. (2018) also find that AGNs exit their high-accretion phase (i.e. the QSO phase) in the most massive galaxy at $z \sim 2$. The absence of QSOs in those massive quenched galaxies means their absence in the most massive haloes. So LRGs, ELGs and QSOs all require the $V_{\rm ceil}$ truncation, which still allows (sub)haloes with large $V_{\rm peak}$ with the help of σ. We need to point out that the actual format of the massive halo incompleteness should not depend solely on $V_{\rm peak}$. This $V_{\rm ceil}$ truncation is chosen as it is the simplest implementation for the incompleteness and it enables a good description of the observed 2-point clustering (See Section 4.1). $v_{\rm smear}$-SHAM and $f_{\rm sat}$-SHAM algorithms then deviate after this step.

For $v_{\rm smear}$-SHAM, we populate a central/satellite galaxy in the centre of each halo/subhalo in the $V_{\rm ceil}$-truncated catalogue from the most massive ones to the least ones until we get the expected number of SHAM galaxies

$$N_{\rm gal} = n_{\rm eff}V_{\rm box}, \tag{14}$$

where $V_{\rm box} = 1\,h^{-3}\,\mathrm{Gpc}^3$ is the box size of the UNIT *N*-body simulation. $n_{\rm eff}$ is the effective number density of the observed sample obtained using equation (5) and the values for each galaxy sample are presented in Table 2. The proper peculiar velocity of the host (sub)haloes $\boldsymbol{v}^h_{\rm pec}$ is also assigned to their galaxies. The velocity of the galaxy along the line of sight $v^g_{\rm pec,Z}$ is then blurred by $v_{\rm smear}$ to mimic the effect of the redshift uncertainty as

$$v^g_{\rm pec,Z} = v^h_{\rm pec,Z} + \begin{cases} \mathcal{N}(0, v_{\rm smear,G}), & \text{Gaussian profile;} \\ \mathcal{L}(0, v_{\rm smear,L}), & \text{truncated Lorentzian profile,} \end{cases} \tag{15}$$

where $v^h_{\rm pec,Z}$ is the component of $\boldsymbol{v}^h_{\rm pec}$ on the *Z*-axis, $\mathcal{N}(0, v_{\rm smear,G})$ and $\mathcal{L}(0, v_{\rm smear,L})$ are a random number sampled by a Gaussian profile

Downloaded from https://academic.oup.com/mnras/article/527/3/6950/7438901 by University College London user on 06 February 2024

or a Lorentzian profile, respectively (as discussed in Section 2.2). As the standard Lorentzian profile is heavy-tailed and subexponential, we remove $\mathcal{L}(0, v_{\rm smear})$ larger than 400 km s^{-1} for LRGs and 2000 km s^{-1} for QSOs. We do not use the $v_{\rm smear}$ parameter in $f_{\rm sat}$-SHAM as explained in Section 4.4.

In $f_{\rm sat}$-SHAM, we further separate haloes and subhaloes from the $V_{\rm ceil}$-truncated catalogue. Only the first $f_{\rm sat}N_{\rm gal}/100$ subhaloes are kept as hosts of ELG satellites and the first $(1-f_{\rm sat})N_{\rm gal}/100$ haloes are for central ELGs. Then, we assign the centre position and the proper peculiar velocity of those selected halo/subhalo to their central/satellite galaxies.

Note that in $v_{\rm smear}$-SHAM, the satellite fraction $f_{\rm sat}$ is defined as the percentage of subhaloes in the list of (sub)haloes selected by SHAM, that is,

$$f_{\rm sat} \equiv \frac{N_{\rm sat}}{N_{\rm gal}} = \frac{N_{\rm sub,SHAM}}{N_{\rm sub,SHAM}+N_{\rm halo,SHAM}}, \tag{16}$$

where $N_{\rm sat}$ is the number of satellite galaxies in the SHAM galaxy catalogue, $N_{\rm sub,\,SHAM} = N_{\rm sat}$ is the number of subhaloes selected by SHAM, and $N_{\rm halo,\,SHAM}$ is the number of haloes selected by SHAM. Note that $f_{\rm sat}$ is different from the percentage of subhaloes in the UNIT simulations:

$$f_{\rm sub} \equiv \frac{N_{\rm sub}}{N_{\rm UNIT}} = \frac{N_{\rm sub}}{N_{\rm sub}+N_{\rm halo}}, \tag{17}$$

where $N_{\rm sub}$ is the total number of subhaloes in the UNIT simulation and $N_{\rm halo}$ is the total number of haloes there.

Finally, we calculate the clustering of model galaxies in redshift space produced by $v_{\rm smear}$-SHAM (LRGs and QSOs) or $f_{\rm sat}$-SHAM (ELGs) and compare it with observations, trying to find the best-fitting parameters. As shown in Appendix A, σ, $V_{\rm ceil}$, $v_{\rm smear}$, and $f_{\rm sat}$ are the primary factors that affect the spatial distribution of DESI dark matter tracers at 5–30 h^{-1} Mpc. Given the well-reproduced clustering (see Section 4.1), we do not explore additional effects such as the assembly bias, which can not be well constrained by our DESI sample due to its low number density (Contreras, Angulo & Zennaro 2021a; Rocher et al. 2023; Yuan et al. 2023a). However, to describe the galaxy–halo connection of dense tracers like the BGS (Pearl et al. 2023), and the cross-correlation between different tracers (Gao et al. 2023; Yuan et al. 2023b), assembly bias will play a role. In addition to the 3-parameter SHAM, we further discuss the performance of the complete 4-parameter SHAM $\{\sigma, V_{\rm ceil}, v_{\rm smear}, f_{\rm sat}\}$ in Appendix A.

3.3 SHAM constraints

We try to find the best-fitting SHAM parameters using a Monte Carlo sampler MULTINEST[4] (Feroz & Hobson 2008; Feroz, Hobson & Bridges 2009; Feroz et al. 2019) assuming a Gaussian likelihood $\mathcal{L}(\Theta)$ for our parameter constraint

$$\mathcal{L}(\Theta) \propto {\rm e}^{-\frac{\chi^2(\Theta)}{2}}. \tag{18}$$

The χ^2 values are obtained as

$$\chi^2(\Theta) = (\boldsymbol{\xi}_{\rm data} - \boldsymbol{\xi}_{\rm model}(\Theta))^T \mathbf{C}^{-1}(\boldsymbol{\xi}_{\rm data} - \boldsymbol{\xi}_{\rm model}(\Theta)), \tag{19}$$

where $\Theta = \{\sigma, V_{\rm ceil}, v_{\rm smear}\}$ for LRG and QSO samples and $\Theta = \{\sigma, V_{\rm ceil}, f_{\rm sat}\}$ for ELG samples. $\boldsymbol{\xi} = (\xi_0, \xi_2)$ denotes the vector composed of the 2PCF monopole and quadrupole. The subscripts 'data' and 'model' of $\boldsymbol{\xi}$ represent measurements from the observational data and SHAM mocks, respectively. $\mathbf{C}$ is the unbiased covariance matrix

Table 1. The priors of $v_{\rm smear}$-SHAM for LRGs and QSOs, and of $f_{\rm sat}$-SHAM for ELGs. Priors of $v_{\rm smear}$-SHAM with a Gaussian profile $v_{\rm smear,\,G}$ are the same with those with $v_{\rm smear,\,L}$.

Tracer	σ	$v_{\rm smear,\,L}$ (km s^{-1})	$V_{\rm ceil}$ (per cent)	$f_{\rm sat}$ (per cent)
LRG	[0,1]	[0,200]	[0,0.15]	/
QSO	[0,2]	[0,1600]	[0,2]	/
ELG	[0,1]	/	[0,20]	[0,30]

that should include the variances of $\boldsymbol{\xi}_{\rm data}$ and $\boldsymbol{\xi}_{\rm model}$. The variances of $\boldsymbol{\xi}_{\rm model}$ can be further decomposed into the cosmic variance of UNIT simulation and the statistical variance due to the random processes included (Section 3.2). The variance of UNIT is considered to be negligible (Section 2.3). $\boldsymbol{\xi}_{\rm model}$ is obtained by averaging the 2PCFs of 32 SHAM galaxy realizations generated using the same Θ with different random seeds. Because the statistical variance of 32 realizations is less than 5 per cent of the observational errors in general, increasing the number would increase the computing cost without much gain in the reliability of the parameter constraint. So $\mathbf{C}$ can be estimated as the variance of $\boldsymbol{\xi}_{\rm data}$ via (Hartlap, Simon & Schneider 2007):

$$\mathbf{C}^{-1} = \mathbf{C}_{\rm s}^{-1}\frac{N_{\rm mocks} - N_{\rm bins} - 2}{N_{\rm mock} - 1}, \tag{20}$$

where $N_{\rm bins} = 20$ (Section 3.1) is the length of $\boldsymbol{\xi}_{\rm data}$, that is, the total number of bins of the monopole and the quadrupole used in the SHAM fitting. $\mathbf{C}_s$ is the jackknife covariance matrix, and is calculated using PYCORR[5] with $N_{\rm mock} = 128$ jackknife subsamples of the observational data. $\mathbf{C}_s$ is thus expressed as

$$\mathbf{C}_{{\rm s},ij} = \frac{1}{N_{\rm mock}-1}\sum_{k=1}^{N_{\rm mock}}[\boldsymbol{\xi}_i^{(k)} - \bar{\boldsymbol{\xi}}_i][\boldsymbol{\xi}_j^{(k)} - \bar{\boldsymbol{\xi}}_j], \tag{21}$$

where $\boldsymbol{\xi}^{(k)}$ is the correlation function measured from the data with the kth jackknife subsample removed, and

$$\bar{\boldsymbol{\xi}}_i = \frac{1}{N_{\rm mock}}\sum_{k=1}^{N_{\rm mock}}\boldsymbol{\xi}_i^{(k)} \tag{22}$$

is the mean 2PCF of all jackknife subsamples. The errors for the data vector are the square root of the diagonal terms of $\mathbf{C}$.

We employ MULTINEST, an efficient nested sampling technique, to constrain Θ. We keep the default convergence criteria which is a tolerance of 0.5 and use 200 particles for the sampling. Using a smaller tolerance or more particles takes more computing time but provides a similar posterior. The prior range for the SHAM fitting is listed in Table 1.

The best-fitting parameters, which are the medians of the 16th and 84th percentiles (the 1σ confidence limit) of the marginalized posterior distributions of individual parameters (Appendix B), their 1σ confidence limits, and the minimum χ^2 are provided by PYMULTINEST[6] (Buchner et al. 2014). All the derived quantities, that is, $f_{\rm sat}$ (in $v_{\rm smear}$-SHAM), HOD, the probability of a (sub)halo to host a central (satellite) galaxy (PDF), the mean halo mass $\langle M_{\rm vir}\rangle$, and the mean $V_{\rm peak}$ $\langle V_{\rm peak}\rangle$ are computed using the nested sampling chain.

[4]https://github.com/farhanferoz/MultiNest

[5]https://github.com/cosmodesi/pycorr

[6]https://github.com/JohannesBuchner/PyMultiNest

Downloaded from https://academic.oup.com/mnras/article/527/3/6950/7438901 by University College London user on 06 February 2024

Table 2. The information for observation and its best-fitting SHAM results of $v_{\rm smear}$-SHAM with Lorentzian redshift uncertainty profile $v_{\rm smear,\,L}$ and $f_{\rm sat}$-SHAM. The columns are: (1) observed tracer type, (2) redshift range, (3) effective redshift calculated using equation (3), (4) redshift of the UNIT simulation snapshot for the SHAM fitting that is close to $z_{\rm eff}$, (5) the effective volume $V_{\rm eff}$ of the observed tracer at the corresponding redshift range obtained with equation (4), (6) the effective number density $n_{\rm eff}$ calculated with equation (5) multiplied by 10^4, the best-fitting parameters, that is, (7) σ, (8) the redshift uncertainty $v_{\rm smear,\,L}$, (9) the massive – (sub)halo incompleteness $V_{\rm ceil}$, (10) the satellite fraction $f_{\rm sat}$, and (11) the minimum χ^2 divided by the degree of freedom. $v_{\rm smear}$ of ELG samples are asserted to 0 and the satellite fraction of LRGs and QSOs is a derived parameter from the nested sampling chain.

tracer type	Redshift range	$z_{\rm eff}$	$z_{\rm UNIT}$	$V_{\rm eff}$ (h^{-3} Gpc^3)	$n_{\rm eff}\times 10^4$ (Mpc^{-3} h^3)	σ	$v_{\rm smear,\,L}$ (km s^{-1})	$V_{\rm ceil}$ (per cent)	$f_{\rm sat}$ (per cent)	χ^2/d.o.f.
LRG	$0.4 < z < 1.1$	0.8138	0.8188	0.150	5.50	$0.27^{+0.09}_{-0.11}$	40^{+9}_{-9}	$0.02^{+0.01}_{-0.01}$	$13.9^{+0.4}_{-0.4}$	24/17
ELG	$0.8 < z < 1.6$	1.2020	1.2200	0.204	7.26	$0.28^{+0.24}_{-0.18}$	/	$3.62^{+0.88}_{-1.10}$	$3.4^{+1.9}_{-1.6}$	22/17
QSO	$0.8 < z < 3.5$	1.7408	1.7710	0.024	0.24	$0.38^{+0.31}_{-0.24}$	215^{+24}_{-31}	$0.23^{+0.11}_{-0.09}$	$12.3^{+0.5}_{-0.5}$	9/17
LRG	$0.4 < z < 0.6$	0.5126	0.5232	0.032	6.16	$0.16^{+0.16}_{-0.11}$	27^{+17}_{-15}	$0.04^{+0.02}_{-0.02}$	$15.2^{+0.5}_{-0.5}$	15/17
LRG	$0.6 < z < 0.8$	0.7067	0.7018	0.052	6.87	$0.25^{+0.07}_{-0.10}$	19^{+12}_{-9}	$0.01^{+0.01}_{-0.01}$	$14.5^{+0.4}_{-0.4}$	23/17
LRG	$0.8 < z < 1.1$	0.9423	0.9436	0.076	4.36	$0.28^{+0.15}_{-0.14}$	30^{+14}_{-12}	$0.04^{+0.03}_{-0.02}$	$13.2^{+0.5}_{-0.5}$	29/17
ELG	$0.8 < z < 1.1$	0.9565	0.9436	0.088	10.47	$0.31^{+0.43}_{-0.21}$	/	$6.68^{+2.17}_{-2.69}$	$5.5^{+2.5}_{-2.2}$	18/17
ELG	$1.1 < z < 1.6$	1.3397	1.3210	0.121	5.13	$0.27^{+0.31}_{-0.17}$	/	$3.07^{+0.80}_{-1.09}$	$4.2^{+2.4}_{-2.1}$	22/17
QSO	$0.8 < z < 1.1$	0.9658	0.9436	0.003	0.29	$0.52^{+0.49}_{-0.30}$	101^{+87}_{-59}	$0.67^{+0.52}_{-0.23}$	$20.1^{+1.2}_{-1.2}$	17/17
QSO	$1.1 < z < 1.6$	1.3665	1.3720	0.009	0.36	$0.32^{+0.49}_{-0.21}$	78^{+35}_{-26}	$0.45^{+0.21}_{-0.21}$	$15.9^{+0.8}_{-0.8}$	11/17
QSO	$1.6 < z < 2.1$	1.8320	1.8330	0.008	0.31	$0.25^{+0.44}_{-0.18}$	273^{+151}_{-61}	$0.26^{+0.09}_{-0.15}$	$11.5^{+0.8}_{-0.8}$	13/17
QSO	$2.1 < z < 3.5$	2.4561	2.4580	0.004	0.13	$0.29^{+0.45}_{-0.18}$	542^{+75}_{-100}	$0.14^{+0.07}_{-0.09}$	$8.1^{+0.7}_{-0.7}$	12/17

4 RESULTS

We present results of $v_{\rm smear}$-SHAM for LRGs and QSOs, $f_{\rm sat}$-SHAM for ELGs for the DESI One Percent Survey in this section. The best-fitting 2PCF, features of the best-fitting σ, $V_{\rm ceil}$, $v_{\rm smear}$, and $f_{\rm sat}$ for different tracers are discussed, respectively. We also check the consistency between the HOD measured from our best-fitting SHAM with those from HOD studies using the same data.

4.1 Clustering

We fit the 2PCF multipoles of the LRG, ELG, and QSO samples from the DESI One Percent Survey at scales of 5–30 h^{-1} Mpc over the redshift range $0.4 < z < 3.5$ with our SHAM algorithms. Table 2 summarizes the best-fitting parameters and their corresponding 1σ confidence intervals, as well as the minimum χ^2 divided by the number of degrees of freedom. Note that $v_{\rm smear}$-SHAM results presented in Table 2, Figs 2–4, and in the appendices all use a Lorentzian $v_{\rm smear,\,L}$. In this case, $f_{\rm sat}$ is obtained as a derived parameter from the Monte Carlo chain.

Figs 2–4 are the 2PCF monopole (first row) and quadrupole (third row) of the observed tracers (filled error bars) and model galaxies/QSOs generated using SHAM with the minimum-χ^2 parameter set (lines with shades). The shaded area around the SHAM clustering is the standard deviation of 2PCFs for all 32 SHAM realizations divided by $\sqrt{32}$. The observed error-rescaled residuals are presented in the second (monopole) and fourth (quadrupole) rows.

The observed clustering of LRG samples is well fitted by $v_{\rm smear}$-SHAM as shown in Fig. 2. The reduced χ^2 value of LRG fitting at $0.8 < z < 1.1$ is around 1.7, which could be explained by underfitting. However, our SHAM LRGs at $0.8 < z < 1.1$ also reproduce w_p at $5 < r_p < 30\,h^{-1}$ Mpc (see Appendix C for the consistent projected 2PCF of SHAM LRGs and observations at this redshift bin). We attribute this large value to the off-diagonal terms in its jackknife covariance matrix. SHAM LRGs at $0.4 < z < 0.8$ have an underestimated ξ_2 at $r > 20\,h^{-1}$ Mpc. At these scales, observations present a plateau while the quadrupoles of SHAM LRGs decrease. This flat quadrupole

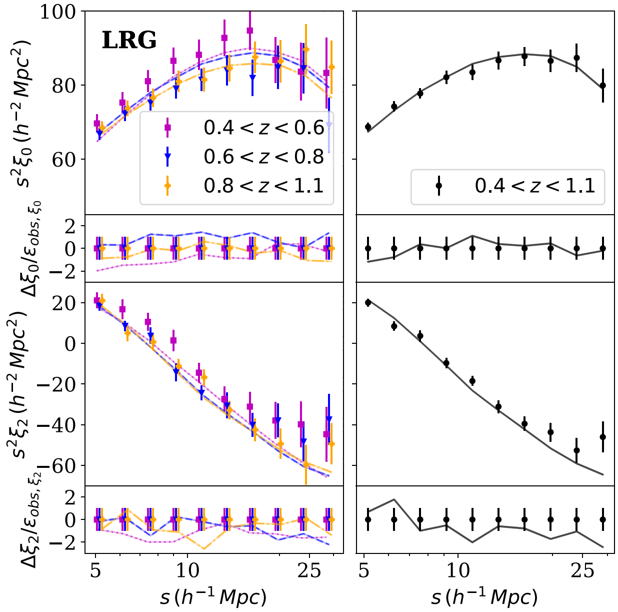

Figure 2. The clustering of observed LRGs (filled error bars) compared with that of the best-fitting SHAM model galaxies with its statistical uncertainty (lines with shades). Monopoles and their residuals normalized by the observed errors $\epsilon_{\rm obs}$ are presented in the first and the second rows. The third and fourth rows present those for quadrupoles. The error bars of data are obtained from 128 jackknife samples, and the statistical uncertainty of SHAM galaxies indicated in the width of the shades is the standard deviation of its 32 realizations divided by $\sqrt{32}$. The uncertainty of best-fitting LRG SHAM galaxies is too small to be seen. Our SHAM provides good fit to the observed clustering at 5–30 h^{-1} Mpc. *The left panel:* the squared, down-triangle, and filled plus markers represents observed LRGs at $0.4 < z < 0.6$, $0.6 < z < 0.8$, $0.8 < z < 1.1$ with slight horizontal shift and the dotted, dashed, dashdot lines corresponds to their best-fit SHAM clustering with the same shift. *The right panel*: the total sample results at $0.4 < z < 1.1$.

Downloaded from https://academic.oup.com/mnras/article/527/3/6950/7438901 by University College London user on 06 February 2024

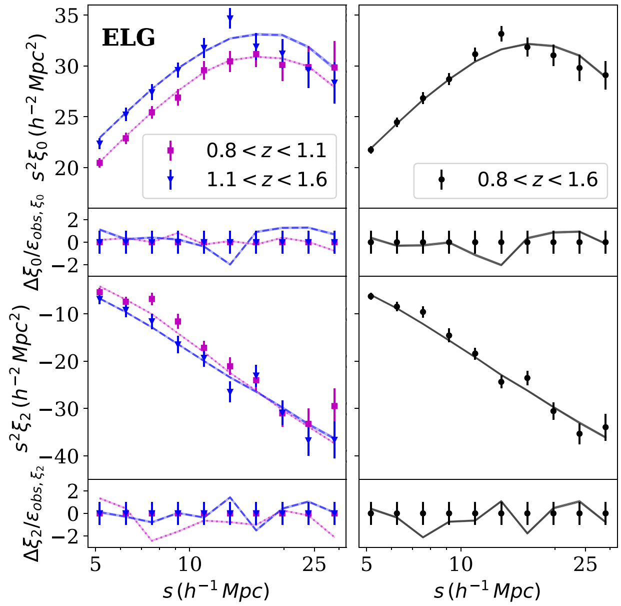

Figure 3. Same as Fig. 2, but for ELGs. *The left panel:* results at $0.8 < z < 1.1$ (squared error bars for observation and dotted lines for SHAM) and $1.1 < z < 1.6$ (down-triangle error bars for observations and dashed lines for SHAM). *The right panel:* results at $0.8 < 1 < 1.6$.

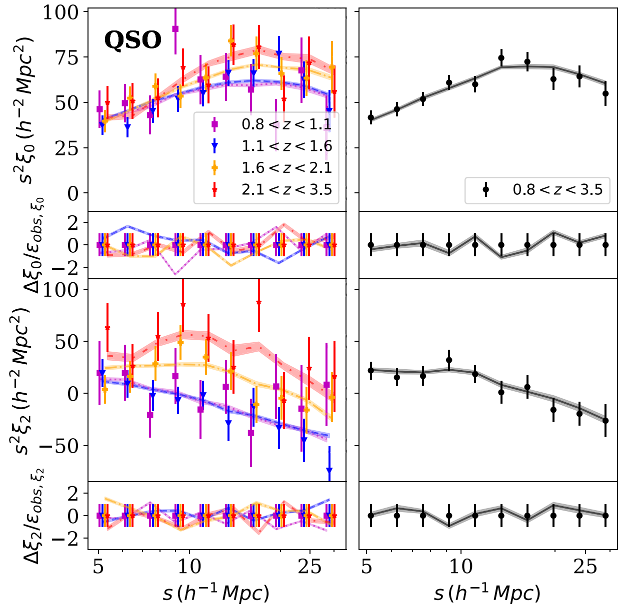

Figure 4. Same as Fig. 2, but for QSOs. *The left panel:* observations at $0.8 < z < 1.1$, $1.1 < z < 1.6$, $1.6 < z < 2.1$, $2.1 < z < 3.5$ (the squared, down-triangle, filled plus, and star markers) and their corresponding best-fit SHAM clustering (and the dotted, dashed, dashdot and dashdotdotted lines). Both with slight horizontal shift. *The right panel:* results at 0.8<z<3.5.

pattern is also present at $20 - 40\,h^{-1}$ Mpc for LRGs from both SDSS-BOSS SGC at $z > 0.4$ and eBOSS LRGs at all redshift bins, even after eliminating all known observational systematics (Ross et al. 2017; Zhao et al. 2021). The observed quadrupole resumes the smooth trend indicated by models at $s > 50\,h^{-1}$ Mpc. Thus, the observed plateau could be attributed to cosmic variance or some uncorrected

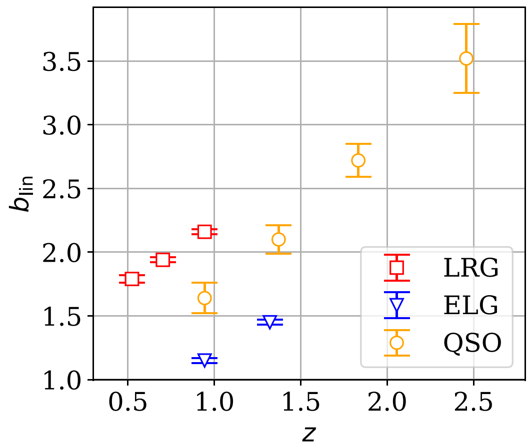

Figure 5. The linear bias of the best-fitting model galaxies and quasars from SHAM with error bars. They are calculated via the power spectrum at $k < 0.05\,h\,\mathrm{Mpc}^{-1}$. For each type of tracer, the linear bias increases with the redshift.

systematics for LRGs at $z > 0.4$. The SHAM underestimation may also indicate some shortcomings in our current understanding of the relationship between (sub)haloes and LRGs as was found in many BOSS and eBOSS galaxy mocks (e.g. Kitaura et al. 2016; Rodríguez-Torres et al. 2016; Zhao et al. 2021; Yu et al. 2022), in particular for red galaxies (Ross et al. 2014). A detailed investigation of this problem is left for future work.

ELG multipoles are well reproduced by SHAM galaxies at all redshift ranges as shown in Fig. 3 and indicated by the reduced χ^2 values in Table 2. QSO clustering has large observed errors due to the small number density of QSOs, which leads to large shot noise. Fig. 4 proves that v_{smear}-SHAM provides a consistently good description of the observation of QSOs in a large redshift range from $z = 0.8$ to 3.5.

With the best-fitting catalogues of SHAM galaxies/quasars, we calculate their power spectrum with PYPOWSPEC[7] for the linear bias b_{lin} via

$$b_{\mathrm{lin}}(z) = \left\langle \left(\frac{P_{\mathrm{g}}(k, z)}{P_{\mathrm{m}}^{\mathrm{lin}}(k, z = 0)} \right)^{\frac{1}{2}} \frac{1}{D(z)} \right\rangle_{k<0.05\,h\,\mathrm{Mpc}^{-1}}, \tag{23}$$

where $P_{\mathrm{g}}(k, z)$ is the power spectrum of SHAM galaxies at redshift z and $P_{\mathrm{m}}^{\mathrm{lin}}(k, z = 0)$ is the linear matter power spectrum used by UNIT simulations renormalized to $z = 0$. Both power spectra are in real space. $D(z)$ is the linear growth rate at redshift z. $k < 0.05\,h\,\mathrm{Mpc}^{-1}$ in equation (23) means that the result is obtained by averaging over this k range.

Fig. 5 presents b_{lin} of LRGs (squares), ELGs (triangles), and QSOs (circles) at different redshifts. The error bars are the weighted standard deviation of the linear bias for SHAM galaxies in the Monte Carlo chain. b_{lin} increases with the redshift for each tracer. This is because we have a constant magnitude cut (DESI Collaboration 2016a), thus we can observe more low-luminosity galaxies/quasars at low redshift compared to the case at high redshift, resulting in an increasing bias with respect to the redshift. Studies using the same DESI EDR data show similar trends and consistent values for b_{lin} (Prada et al. 2023; Rocher et al. 2023; Yuan et al. 2023a).

[7] https://github.com/dforero0896/pypowspec

Downloaded from https://academic.oup.com/mnras/article/527/3/6950/7438901 by University College London user on 06 February 2024

4.2 Scatter σ in galaxy–halo mass relation

As discussed in Yu22, σ in our $v_{\rm smear}$-SHAM is composed of the intrinsic scatter in the galaxy–halo mass relation and the completeness for galaxies with an intermediate stellar mass. For LRG samples, $\sigma \sim 0.2$ dex. However, since there is a degeneracy between σ and $V_{\rm ceil}$ (see Appendix B for the posteriors of LRGs), it is not clear whether there is a redshift evolution in σ. For ELG samples, the constraints in σ are weak regardless of the prior range. Given its large number density, this is not the result of large errors in clustering, as is the case for QSOs. The (sub)halo incompleteness of ELGs is related to their incompleteness in stellar mass and in luminosity (Favole et al. 2016; Gonzalez-Perez et al. 2020). This leads to a complex galaxy property–halo mass connection for ELGs, thus a weakly constrained σ as it integrates many factors. σ also leads to the stochastic variance in the clustering of SHAM galaxies. For the LRG and ELG samples, this variance is as small as 5 per cent of the observational error $\epsilon_{\rm obs}$ (not visible as shown in Figs 2 and 3). So we can also ignore its effect on the final χ^2 values in general.

4.3 Massive (sub)halo incompleteness $V_{\rm ceil}$

For LRGs, $V_{\rm ceil}$ describes the halo/stellar mass incompleteness at the massive end. As shown in LRG posteriors (See Appendix B), $V_{\rm ceil}$ values for LRGs are very small, but are definitely non-zero at 1σ level. This incompleteness can be attributed to the fact that the target selection of LRGs removes some of the most massive blue galaxies, leading to empty massive haloes.

For ELG samples, $V_{\rm ceil}$ is critical to describe their absence in the centre of massive (sub)haloes. ELG entries in Table 2 show that we shall remove a per cent level of (sub)haloes, allowing few (sub)haloes with $V_{\rm peak} > 300\,{\rm km\,s^{-1}}$ to host an ELG at their centre (Fig. 13). Since there is no degeneracy among parameters of the $f_{\rm sat}$-SHAM, the $1-\sigma$ difference between the $V_{\rm ceil}$ of ELGs at $0.8 < z < 1.1$ and $1.1 < z < 1.6$ embodies their clustering difference.

QSOs at $0.8 < z < 1.1$ show a larger $V_{\rm ceil}$ than that of QSOs at higher redshifts, but this difference is not significant due to the weak constraint. This is consistent with Chaussidon et al. (2023) in which QSOs at $z < 1.0$ show a smaller purity than those at high redshifts. Even though $V_{\rm ceil}$ for QSOs only exclude less than 1 per cent of (sub)haloes with the largest $V_{\rm scat}$ (equation 13), the clustering of QSOs cannot be well fitted without the $V_{\rm ceil}$ parameter. As explained in Section 3.2, this is consistent with findings of SAM studies (e.g. Griffin et al. 2019) and observations (e.g. Uchiyama et al. 2018), in which QSOs are absent in the centre of the most massive (sub)haloes.

4.4 Redshift uncertainty $v_{\rm smear}$

$v_{\rm smear}$-SHAM uses a Lorentzian $v_{\rm smear,\,L}$ by default as this is a good model for DESI tracers in general. In particular, for LRGs, Lorentzian and Gaussian profiles can both describe the redshift difference distribution of LRG repeat observations (Fig. 1). So we perform $v_{\rm smear}$-SHAM fitting with Gaussian $v_{\rm smear,\,G}$ as well and Table 3 includes the best-fitting results. The χ^2 values of SHAM with $v_{\rm smear,\,G}$ are similar to those of SHAM with $v_{\rm smear,\,L}$. Their best-fitting σ and $V_{\rm ceil}$ are also consistent with each other, meaning that the clustering effect of a truncated Lorentzian $v_{\rm smear,\,L}$ and a Gaussian $v_{\rm smear,\,G}$ is almost equivalent. So we need to check the $v_{\rm smear}$ consistency with the statistical redshift uncertainty estimated from repeat observations.

Fig. 6 is the comparison between the best-fitting SHAM $v_{\rm smear}$ (filled error bars) and the best-fitting redshift uncertainty measured from repeat observations (em pty error bars) for DESI LRGs (left panel) and QSOs (right panel). The results of Lorentzian profiles are in star markers and those of Gaussian profiles are in squared markers. In particular, Gaussian profiles for LRGs are vertically shifted. The best-fitting LRG SHAM $v_{\rm smear,\,G}$ values agree with the Gaussian dispersion $\sigma_{\Delta v}$ of repeat observations, while SHAM $v_{\rm smear,\,L}$ values underestimate the statistical redshift uncertainty evaluated using the width of Lorentzian functions $w_{\Delta v}$. Note that the standard deviation $\hat{\sigma}_{\Delta v}$ of LRG repeats are also consistent with the dispersion of the Gaussian profile. Therefore, the Gaussian profile $v_{\rm smear,\,G}$ is more suitable for illustrating the uncertainty of the redshift of LRGs in redshift bins.

Table 3. The best-fitting results of the $v_{\rm smear}$-SHAM fitting for LRGs with Gaussian $v_{\rm smear,\,G}$.

Redshift range	σ	$v_{\rm smear,\,G}$ (${\rm km\,s^{-1}}$)	$V_{\rm ceil}$ (per cent)	$f_{\rm sat}$ (per cent)	χ^2/d.o.f.
$0.4 < z < 1.1$	$0.21^{+0.14}_{-0.10}$	95^{+12}_{-14}	$0.03^{+0.02}_{-0.02}$	$14.7^{+0.3}_{-0.3}$	24/17
$0.4 < z < 0.6$	$0.14^{+0.11}_{-0.08}$	67^{+28}_{-30}	$0.04^{+0.02}_{-0.02}$	$15.2^{+0.4}_{-0.4}$	15/17
$0.6 < z < 0.8$	$0.31^{+0.04}_{-0.06}$	42^{+16}_{-22}	$0.00^{+0.01}_{-0.00}$	$14.7^{+0.3}_{-0.3}$	23/17
$0.8 < z < 1.1$	$0.28^{+0.19}_{-0.17}$	84^{+17}_{-18}	$0.04^{+0.03}_{-0.03}$	$14.7^{+0.3}_{-0.3}$	30/17

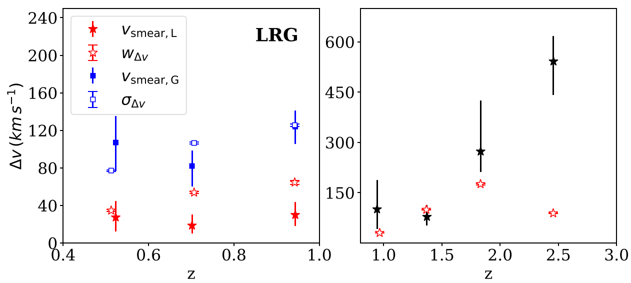

Figure 6. The redshift uncertainty quantified by the best-fitting SHAM $v_{\rm smear}$ (filled error bars) and that estimated statistically by the repeat observation Δv (empty error bars) for galaxies in different redshift slices. The results of Lorentzian profiles are star markers and those of Gaussian profiles are in square markers. For DESI LRGs, SHAM $v_{\rm smear,\,L}$ are systematically lower than $w_{\Delta v}$. In the case of the Gaussian profile, the SHAM $v_{\rm smear,\,G}$ and $\sigma_{\Delta v}$ (both with vertical offsets) agree with each other. For QSOs, the statistical uncertainty $w_{\Delta v}$ is not consistent with the SHAM $v_{\rm smear,\,L}$ at $z > 1.5$.

In contrast, the Lorentzian profile results ($w_{\Delta v} = 46.5 \pm 0.8\,{\rm km\,s^{-1}}$, while $v_{\rm smear,L} = 40 \pm 9\,{\rm km\,s^{-1}}$) are in better agreement for LRGs in the full redshift range, indicating that there are multiple types of LRGs with different redshift uncertainty properties. As a result, Chaussidon et al. (2023) and Raichoor et al. (2023) use a linear combination of Gaussian profiles to fit the redshift difference Δv. Nevertheless, a truncated Lorentzian with just one parameter works in the same way as multiple-Gaussian profiles in terms of the clustering effects and SHAM results.

For QSOs in the right panel of Fig. 6, SHAM $v_{\rm smear,\,L}$ shows a non-decreasing trend. This reflects the quadrupole amplitude of QSOs at different redshift bins shown in the third row of Fig. 4. However, this trend is inconsistent with that of repeat observations (empty star error bars), and SHAM $v_{\rm smear,\,L}$ starts to deviate from $w_{\Delta v}$ of repeat observations at $z \gtrsim 1.5$. The discrepancy is possibly due to the switch of the main spectral line for redshift determination from Mg II and C IV (Zarrouk et al. 2018). QSO spectral lines are subject to systematical velocity shifts caused by astrophysical effects (e.g. Gaskell 1982; Richards et al. 2002, 2011) and repeat observations for the same object cannot capture this shift. But this shift is different

Downloaded from https://academic.oup.com/mnras/article/527/3/6950/7438901 by University College London user on 06 February 2024

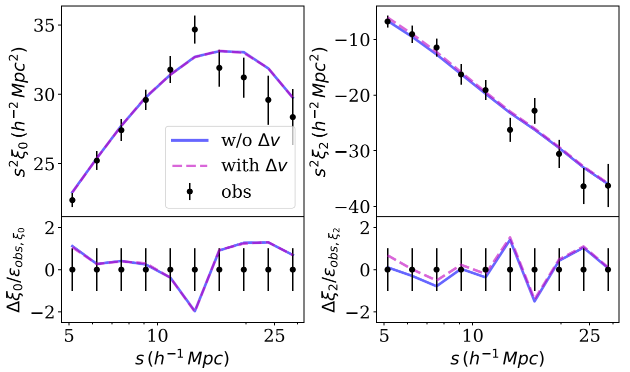

Figure 7. The effect of the maximum ELG redshift uncertainty $w_{\Delta v} = 13.4\,\mathrm{km\,s^{-1}}$ on the 2PCF monopole (left) and quadrupole (right). Multipoles of SHAM galaxies without $v_{\rm smear,L}$ are in solid lines, the ones with $v_{\rm smear,L} = 13.4\,\mathrm{km\,s^{-1}}$ are in dashed lines. Data are plotted in filled circles with error bars and the residuals normalized by the observed error bars are presented in the second row. No significant clustering effect is induced by the largest redshift uncertainty of ELGs at 5–30 h^{-1} Mpc.

from object to object, creating an extra relative random motion between QSO pairs. Moreover, Shen et al. (2016) have proved that Mg II is the least shifted broad emission of QSOs, while C IV can be strongly shifted. This will result in a larger random motion between QSO pairs at $z > 1.5$ than those at $z < 1.5$. This motion is integrated into $v_{\rm smear,L}$ of SHAM, resulting in its fast rise at $z > 1.5$ and explaining the inconsistency between $v_{\rm smear,L}$ and $w_{\Delta v}$.

The redshift uncertainty of ELGs is small in general as presented in Fig. 1. Its largest redshift uncertainty among ELGs samples, that is, $v_{\rm smear,L} = 13.4\,\mathrm{km\,s^{-1}}$ for ELGs at $1.1 < z < 1.6$, does not produce a significant clustering effect, as illustrated in Fig. 7. The solis line is the clustering of SHAM galaxies created using the best-fitting $f_{\rm sat}$-SHAM. The dashed line shows the clustering with $v_{\rm smear,L} = 13.4\,\mathrm{km\,s^{-1}}$ applied to the peculiar velocity of the best-fitting $f_{\rm sat}$-SHAM ELGs. For the monopole, $v_{\rm smear,L}$ have little influence as expected, and the influence on the quadrupole is restricted to 5–8 h^{-1} Mpc and is within 1σ range of the observed jackknife error bars. Therefore, asserting $v_{\rm smear} = 0$ for $f_{\rm sat}$-SHAM does not bias the best-fitting results of the other three parameters.

4.5 Satellite fraction $f_{\rm sat}$

The fraction of satellites, $f_{\rm sat}$, for LRGs and QSOs, is calculated when σ and $V_{\rm ceil}$ are given to $v_{\rm smear}$-SHAM. We present in Fig. 8 the impact of σ, $V_{\rm ceil}$ and the number density $n_{\rm eff}$ on $f_{\rm sat}$ for SHAM galaxies produced by $v_{\rm smear}$-SHAM at $z = 0.94$ (circled error bars) and $z = 1.83$ (triangle error bars). The $f_{\rm sub}$ of UNIT simulations at those redshifts are plotted in horizontal lines, obtained using equation (17). The fixed parameters[8] are $\sigma = 0.1$, $V_{\rm ceil} = 0.1$, $n_{\rm eff} = 4\times10^{-4}\,\mathrm{Mpc^{-3}}\,h^3$. $f_{\rm sat}$ monotonically increases with σ, $V_{\rm ceil}$, and $n_{\rm eff}$. This is because larger σ, $V_{\rm ceil}$, and $n_{\rm eff}$ all mean selecting more (sub)haloes with small $V_{\rm peak}$, corresponding to a larger fraction of subhaloes/satellites. In contrast, for σ, $V_{\rm ceil} \sim 0$, there are a few selected subhaloes that have a large $V_{\rm peak}$, resulting in $f_{\rm sat} < f_{\rm sub}$. Due to the tight constraints on LRG σ and $V_{\rm ceil}$, the 1σ confidence interval of LRG $f_{\rm sat}$, which is a derived parameter, is also small. From another aspect, the slope of the $f_{\rm sat}$–σ and $f_{\rm sat}$–$V_{\rm ceil}$ relations decreases as σ and $V_{\rm ceil}$ become larger. Additionally, the slope of the $f_{\rm sat}$–$n_{\rm eff}$ relation increases with $n_{\rm eff}$. The combination of these effects results in the small errors of QSO $f_{\rm sat}$ despite its loose constraints on σ and $V_{\rm ceil}$.

The satellite fraction of $v_{\rm smear}$-SHAM is also affected by the redshift, that is, the substructure growth. $f_{\rm sat}$ of SHAM galaxies at $z = 1.83$ are lower than those at $z = 0.94$, calculated with the same $v_{\rm smear}$-SHAM parameters. This is consistent with the decreasing trend of $f_{\rm sat}$ for LRGs and QSOs with the redshift.

For ELGs, we find that about 4 per cent of them are satellite galaxies when we fit the data with our $f_{\rm sat}$-SHAM method. Such a low fraction of satellites is also found in models mimicking a DESI-like survey (Gonzalez-Perez et al. 2018). In the literature, for different selections of ELGs, this fraction has been found to range from $f_{\rm sat} \sim 5$ to $\sim$22.5 per cent (Favole et al. 2016; Gao et al. 2022) in VIMOS Public Extragalactic Redshift Survey (VIPERS; Scodeggio et al. 2018) and from $\sim$17 per cent (Guo et al. 2019) to 19.3 per cent (Lin et al. 2023) in eBOSS. The difference in the strength of the [O II] emission can also alter $f_{\rm sat}$. For example, Gonzalez-Perez et al. (2018) and Gao et al. (2022) find that strong [O II] emitters tend to have a low $f_{\rm sat}$ down to per cent level, that is, 4.6 per cent and 7.0 ± 2.0 per cent, respectively. In Fig. 9, we show the distribution of DESI ELG [O II] fluxes, $F_{\rm [O\,II]}$, and luminosities, $L_{\rm [O\,II]}$, as a function of redshift. We find that more than 71 per cent of DESI ELGs from the One Percent Survey have $F_{\rm [O\,II]} > 10^{-16}\,\mathrm{erg\,s^{-1}\,cm^{-2}}$ (the dashed line on the left panel), which is the cut assumed in the theoretical study of Gonzalez-Perez et al. (2018). On the right panel, 24 per cent of them are strong [O II] emitters according to the definition in Gao et al. (2022), that is, they should have $L_{\rm [O\,II]}$ larger than

$$\log_{10} L^{\rm thres}_{\rm [O\,II]}(z) = \log_{10} L^{\rm thres}_{\rm [O\,II]}(z=0.5) + \log_{10}\left(\frac{1+z}{1+0.5}\right)^{\beta_L}, \quad (24)$$

where $z \in (0.8, 1.6)$, and $L^{\rm thres}_{\rm [O\,II]}(z=0.5) = 10^{41.75}\,\mathrm{erg\,s^{-1}}$, which is the $L_{\rm [O\,II]}$ lower bound of VIPERS ELGs with $f_{\rm sat} = 7.0 \pm 2.0$ per cent. This fraction for VIPERS and eBOSS are 10 per cent and 12 per cent, respectively. Thus, it is reasonable if we obtain a smaller $f_{\rm sat}$ from the DESI data, compared to that of the eBOSS ELGs and VIPERS samples.

However, it is still possible that our satellite fraction is underestimated as we do not include orphan galaxies that are necessary for correcting the deficits of the current subhalo tracking method (Behroozi et al. 2019). We check in Appendix D the consistency between the $f_{\rm sat}$ measured by $f_{\rm sat}$-SHAM and galaxy mocks provided by UniverseMachine (Behroozi et al. 2019) and SAM models (Gonzalez-Perez et al. 2018). The mass resolution of the UNIT simulation may also not be good enough to resolve all substructures for ELGs. Moreover, $f_{\rm sat}$ is model dependent (e.g. Favole et al. 2016; Gao et al. 2022). In studies for DESI ELGs, Gao et al. (2023) present a redshift- and stellar-mass-dependent satellite fraction with reconstructed orphan galaxies. Rocher et al. (2023) find that adding conformity can lead to a smaller $f_{\rm sat}$ compared to HOD without that. So it is difficult to compare fairly the $f_{\rm sat}$ value provided by different models for different galaxy surveys. We will leave those for future work.

In Fig. 10, we present the satellite fraction $f_{\rm sat}$ as a function of the (parent) halo mass $M_{\rm vir}$. For LRGs and QSOs, almost all galaxies residing on small haloes selected by SHAM are satellites, and then $f_{\rm sat}$ decreases to 0 as $M_{\rm vir}$ increases to $8.9\times10^{13}\,h^{-1}\,\mathrm{M_\odot}$ for LRGs and $1.8\times10^{13}\,h^{-1}\,\mathrm{M_\odot}$ for QSOs. For ELGs, less than half of the selected small haloes host satellites, then the satellite fraction decreases to 0 as $M_{\rm vir} > 2.2\times10^{12}\,h^{-1}\,\mathrm{M_\odot}$.

[8] These are typical values for LRGs. We have checked the $f_{\rm sat}$ relations with typical values for QSOs and found the same trends as in Fig. 8.

Downloaded from https://academic.oup.com/mnras/article/527/3/6950/7438901 by University College London user on 06 February 2024

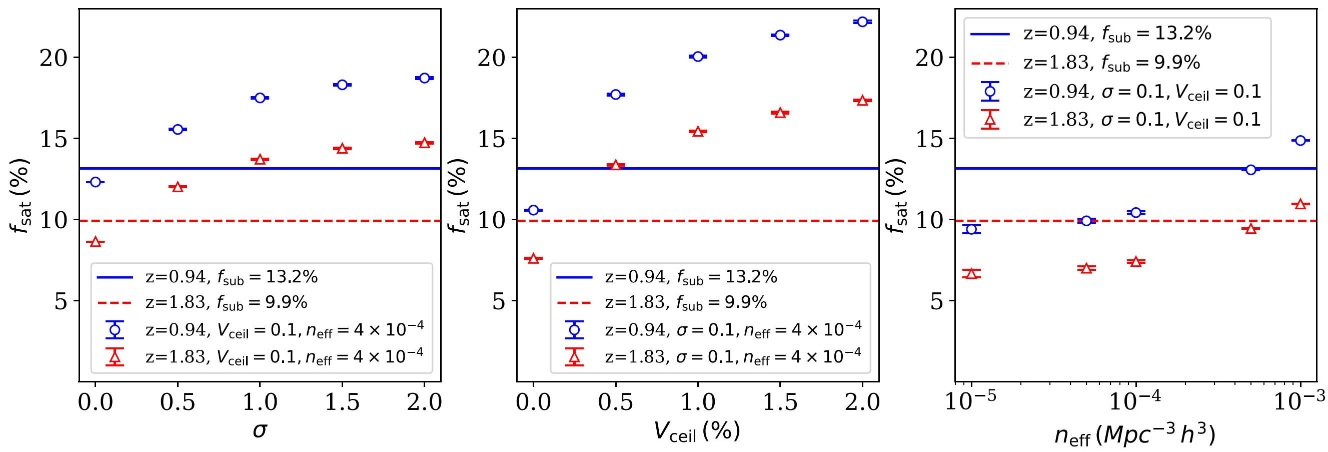

Figure 8. $f_{\rm sat}$ evolution with σ (left panel), $V_{\rm ceil}$ (middle panel), and $n_{\rm eff}$ (right panel) for model galaxies of SHAM at $z = 0.94$ (triangle error bars) and those at $z = 1.83$ (circle error bars) produced by $v_{\rm smear}$-SHAM. We present the dependence of $f_{\rm sat}$ with one parameter and fix the other two parameters (typical values for LRGs) as indicated in the label. The error bar of $f_{\rm sat}$ is the standard deviation of $f_{\rm sat}$ among 32 realizations. The subhalo fraction of the UNIT simulation at $z = 0.94$ (dashed lines) and $z = 1.83$ (solid lines) defined in equation (17) is plotted in dashed lines.

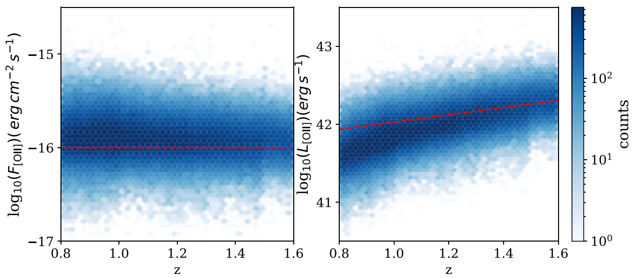

Figure 9. The flux (in erg cm^{-2} s^{-1}) and the luminosity (in erg s^{-1}) of [O II] emission for ELGs as a function of the redshift. The dashed lines are the strong [O II] emitter thresholds. The line on the left represents the standard of Gonzalez-Perez et al. (2018) with $F_{\rm [O\,II]} > 10^{-16}$ erg s^{-1} cm^{-2}. The one on the right shows an evolving $L^{\rm thres}_{\rm [O\,II]}$ (equation 24) derived from Gao et al. (2022). 71 per cent of DESI ELGs pass the $F_{\rm [O\,II]}$ selection, 24 per cent pass the $L_{\rm [O\,II]}$ selection.

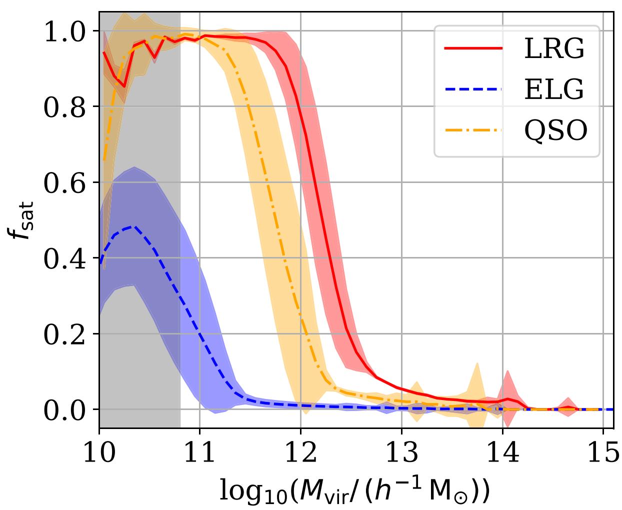

Figure 10. The $f_{\rm sat}$–$M_{\rm vir}$ relation of SHAM LRGs at $0.4 < z < 1.1$ (the solid line), ELGs at $0.8 < z < 1.6$ (the dashed line), and QSOs at $0.8 < z < 3.5$ (the dashdotted line). The shaded areas around lines indicates the 1σ errors of the $f_{\rm sat}$–$M_{\rm vir}$ relation are derived from the Monte Carlo chain. The vertical shades show $M_{\rm vir} < 6\times10^{10}\,h^{-1}\,{\rm M}_\odot$ where halo mass measurement is no longer reliable (Section 2.3).

4.6 Halo occupation distribution

Fig. 11 shows the average HOD of SHAM LRGs with Lorentzian $v_{\rm smear,\,L}$ at $0.4 < z < 1.1$, SHAM ELGs at $0.8 < z < 1.6$, and SHAM QSOs at $0.8 < z < 3.5$ as a function of the halo mass $M_{\rm vir}$. They are computed with the weights from the Monte Carlo chain. $M_{\rm vir}$ corresponds to the virial mass of host haloes or parent haloes of subhaloes. We opt not to compare directly our halo occupation with the other DESI EDR galaxy–halo connection results. This is because our HODs originate from different N-body simulations, varying in redshift, halo finders, and mass resolution. These differences might influence the HOD configuration. Consequently, rather than pursuing a direct comparison of HOD, our target in the following section is to conclude the common features of DESI EDR tracers measured by different galaxy–halo connection methods and the characteristics of different tracers provided by our SHAM.

For LRGs, their stellar mass is closely related to the halo mass (e.g. Leauthaud et al. 2012; Behroozi et al. 2019). Their HOD can be modelled using a 5-parameter form, with a smoothed step function for central galaxies, and a power law for satellites (e.g. Zheng et al. 2005; Zhai et al. 2017). The HOD of our central SHAM LRGs reaches $\langle N\rangle = 0.75 \pm 0.07$ at $M_{\rm vir} = 10^{13.3}\,h^{-1}\,{\rm M}_\odot$ and decreases towards the massive end as we set $V_{\rm ceil}$ free. This incompleteness is consistent with the measurement of AbacusSummit HOD for DESI LRGs (Yuan et al. 2023a).

There are various HOD models for central ELG. Avila et al. (2020) and Rocher et al. (2023) discuss several ELG central profiles: the modified high-mass-quenched model (Alam et al. 2020), the Gaussian function, the star-forming HOD model (Avila et al. 2020), and the lognormal HOD model (Rocher et al. 2023). The central HOD of our SHAM ELGs shows a preference for a star-forming HOD profile with a turning point at $M_{\rm vir} = 10^{11.7}\,h^{-1}\,{\rm M}_\odot$ that reaches $\langle N\rangle = 0.06 \pm 0.03$. ELGs residing in $M_{\rm vir} > 10^{12.5}\,h^{-1}\,{\rm M}_\odot$ are also found in the study of Gao et al. (2023).

There are also multiple profiles for QSO HOD models (Smith et al. 2020; Yuan et al. 2023a). Our central QSO HOD reaches the maximum value $\langle N\rangle = 0.016 \pm 0.001$ after $M_{\rm vir} = 10^{12.4}\,h^{-1}\,{\rm M}_\odot$. Note that no tracer reaches $\langle N\rangle = 1$. It means that we will not find one galaxy/QSO in every halo above a certain halo mass. It is consistent with the $V_{\rm ceil}$ results that LRGs from the One Percent Survey are not

Downloaded from https://academic.oup.com/mnras/article/527/3/6950/7438901 by University College London user on 06 February 2024

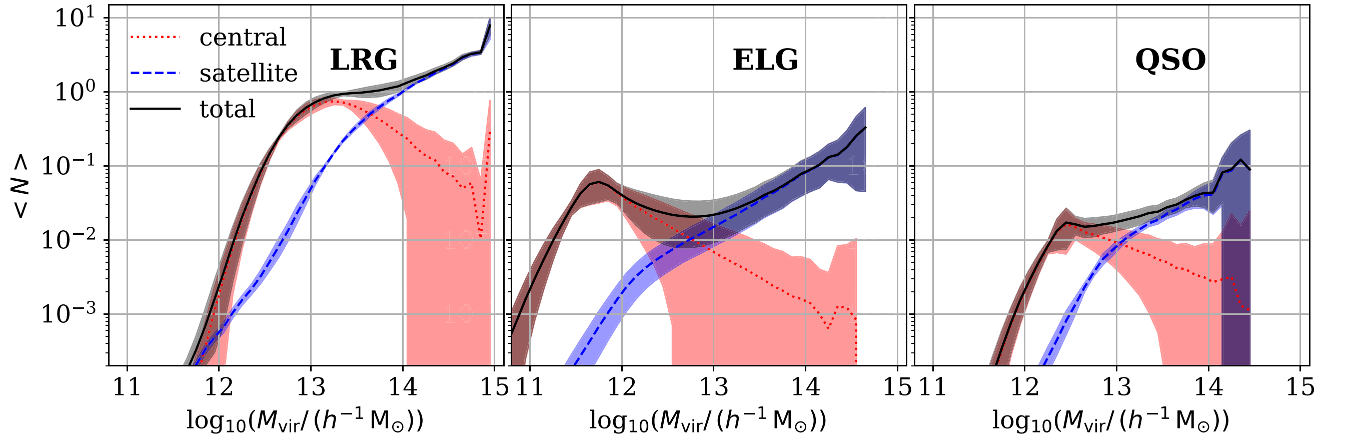

Figure 11. The average HOD of SHAM LRGs at $0.4 < z < 1.1$ (left panel), ELGs at $0.8 < z < 1.6$ (middle panel), and QSOs at $0.8 < z < 3.5$ (right panel). The contribution of central galaxies to the HOD is shown by dotted lines and that of satellites by dashed lines. The 1σ errors derived from the Monte Carlo chain are shown as shaded regions around lines.

Table 4. The best-fitting α, β, $M_{\rm trun}$ of $\langle N_{\rm sat}\rangle$, the mean haloe mass $\langle M_{\rm vir}\rangle$, and the mean $V_{\rm peak}$ $\langle V_{\rm peak}\rangle$ for LRGs at $0.4 < z < 1.1$, ELGs at $0.8 < z < 1.6$ and QSOs at $0.8 < z < 3.5$.

Tracer	α	β	$\log_{10}(M_{\rm turn})$ ($h^{-1}\,{\rm M}_\odot$)	$\log_{10}(\langle M_{\rm vir}\rangle)$ ($h^{-1}\,{\rm M}_\odot$)	$\langle V_{\rm peak}\rangle$ (km s^{-1})
LRG	$0.70^{+0.01}_{-0.01}$	$1.97^{+0.01}_{-0.01}$	$13.55^{+0.00}_{-0.00}$	13.18 ± 0.01	457 ± 6
ELG	$0.76^{+0.06}_{-0.07}$	$2.16^{+0.13}_{-0.14}$	$12.05^{+0.20}_{-0.20}$	11.90 ± 0.06	159 ± 4
QSO	$0.73^{+0.07}_{-0.07}$	$2.13^{+0.05}_{-0.05}$	$12.95^{+0.10}_{-0.10}$	12.59 ± 0.03	346 ± 8

complete, while ELGs and QSOs are absent from massive haloes due to physical reasons.

Note that our SHAM model galaxies/quasars present a decreasing number of centrals in the massive halo in Fig. 11 (dashed lines with shades). This is because we apply a simple, empirical truncation to the massive haloes via $V_{\rm ceil}$, aiming at recover the autocorrelations of the DESI EDR tracers with a minimum number of parameters. Therefore, the increasing incompleteness at the massive end for model galaxies is not necessarily physical, given the lack of assembly bias effect for example. In fact, Rocher et al. (2023) find a similar decreasing trend for central ELGs in DESI with four different models that include the assembly bias. Meanwhile, Yuan et al. 2023a provide a constant number of central galaxies/quasars in massive haloes and find incompleteness there for both LRGs and QSOs from DESI, with the HOD models including the assembly bias. Nevertheless, the fact that all these galaxy/quasar–halo connection models show a central galaxy occupation below unity regardless of the assembly bias suggests that LRGs, ELGs, and QSOs from the DESI One Percent Survey are likely incomplete in their host halo masses. We will need a more sophisticated galaxy–halo relation as well as better observations and simulations to understand this incompleteness better.

The average HOD of our SHAM satellites for all tracers can be fitted by two exponential functions of $M_{\rm vir}$, that is,

$$\langle N_{\rm sat}\rangle \propto \begin{cases} M_{\rm vir}^{\alpha}, & M_{\rm vir} > M_{\rm turn}. \\ M_{\rm vir}^{\beta}, & M_{\rm vir} < M_{\rm turn}. \end{cases} \tag{25}$$

The best-fitting results obtained by PYMULTINEST are presented in Table 4. The second exponent β at a lower mass range for all tracers is consistent and around 2. Though $M_{\rm turn}$ values are different for different tracers, their slope in the massive end α is well consistent

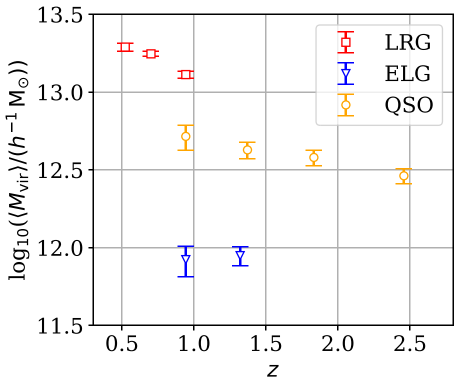

Figure 12. The evolution of the mean parent halo mass $\langle M_{\rm vir}\rangle$ of SHAM LRGs with Gaussian $v_{\rm smear,\,G}$ (squares error bars), ELGs (triangle error bars), and QSOs (circle error bars) obtained for subsamples at redshift slices as a function of redshift. There are three ranges of mean mass and the values of LRGs and QSOs decrease with redshift.

with 0.7. This is consistent with ELG HOD slopes in Rocher et al. (2023) but smaller than those from LRG HOD in Yuan et al. 2023a.

The mean parent halo mass $\langle M_{\rm vir}\rangle$, derived from the Monte Carlo chain as introduced in Section 3.3, is shown in Table 4. Those values are consistent with those of ABACUSSUMMIT HOD using the same data from the DESI One Percent Survey (Rocher et al. 2023; Yuan et al. 2023a). Fig. 12 is the evolution of the mean parent halo mass for SHAM LRGs with Gaussian $v_{\rm smear,\,G}$, ELGs, and QSOs. $\langle M_{\rm vir}^{\rm LRG}\rangle$ is not smaller than $10^{13}\,h^{-1}\,{\rm M}_\odot$, and $\langle M_{\rm vir}^{\rm QSO}\rangle$ values range from $10^{12.2}$ to $10^{12.7}\,h^{-1}\,{\rm M}_\odot$. Both decrease with redshift, consistent with the redshift-evolution HOD results from Yuan et al. 2023a. For ELG parent halo, there is no significant evolution and both $\langle M_{\rm vir}\rangle$ are below $10^{12}\,h^{-1}\,{\rm M}_\odot$. Rocher et al. (2023) and Gao et al. (2023) also find the same feature for the mean halo mass of ELGs but with slightly different values. Those are all consistent with the expectation of DESI Collaboration (2016a). But the bias of ELGs still increases with redshift as indicated in Fig. 5. It should be noted that only 1.6 per cent of ELGs and less than 0.03 per cent of LRGs and QSOs reside in haloes lower than the reliable mass threshold $6 \times 10^{10}\,h^{-1}\,{\rm M}_\odot$ (Section 2.3). So the influence of the limitation in the N-body simulation halo finder on our SHAM study can be dismissed.

Downloaded from https://academic.oup.com/mnras/article/527/3/6950/7438901 by University College London user on 06 February 2024

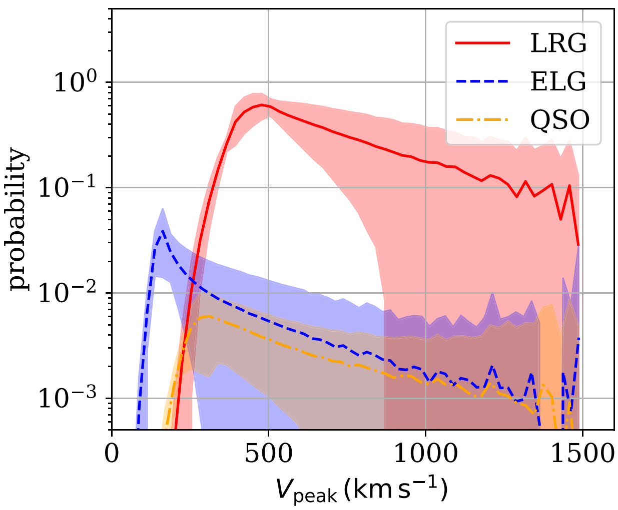

Figure 13. The probability of a (sub)halo to host an LRG (the solid line), an ELG (the dashed line), or a QSO (the dashdotted line) as a function of $V_{\rm peak}$ of (sub)haloes for LRGs with Gaussian $v_{\rm smear,\,G}$, ELGs and QSOs at $0.8 < z < 1.1$. The shades around lines are their 1σ errors calculated using the Monte Carlo chain.

The PDF of (sub)halo $V_{\rm peak}$ that can host a central (satellite) galaxy is shown in Fig. 13 for all three tracers at $0.8 < z < 1.1$. This is the empirical galaxy–halo relation that we calibrate using SHAM described in Section 3.2, that is, LRG with Gaussian $v_{\rm smear,\,G}$, ELG, and QSO. The shape of the PDF is modulated indirectly by σ and $V_{\rm ceil}$. ELGs mainly reside in (sub)haloes with $V_{\rm peak} \lesssim 200$ km s^{-1}, while LRG and QSOs are populated in haloes with $V_{\rm peak} > 200$ km s^{-1}. The PDFs of LRGs and ELGs present a clear peak, while the probability of QSOs in the massive end decays slower than them. The probability patterns for different tracers can be used as a reference for future multitracer studies. The mean $V_{\rm peak}$ values for the total LRG, ELG, and QSO samples are presented in Table 4.

5 CONCLUSIONS

We have generated catalogues of mock galaxies matching the clustering of dark tracers from the DESI One Percent Survey in the range of 5–30 h^{-1} Mpc. The DESI samples studied here are LRGs at $0.4 < z < 1.1$; ELGs at $0.8 < z < 1.6$, and QSO at $0.8 < z < 3.5$ (Section 2.1). Mock galaxies are painted on the dark matter only UNIT simulation (Section 2.3), using two SHAM algorithms (Section 3.2). The first algorithm, $v_{\rm smear}$-SHAM, is used for LRGs and QSOs, and has the following free parameters: σ, to model the dispersion in the galaxy–halo mass relation but also include the incompleteness of halo mass; $V_{\rm ceil}$, to account for the incompleteness of massive haloes for the galaxy samples; and $v_{\rm smear}$, to model the uncertainty in the redshift determination process. The other SHAM model, $f_{\rm sat}$-SHAM with a free satellite fraction $f_{\rm sat}$, is introduced here to model ELGs as $f_{\rm sat}$ is crucial to recover the quadrupole of DESI ELGs. The redshift uncertainty of ELGs is the lowest among the considered tracers and its $v_{\rm smear}$ has a negligible impact on the clustering of SHAM ELGs down to 5 h^{-1} Mpc. So $v_{\rm smear}$ is not included in $f_{\rm sat}$-SHAM.

For LRGs, we find the best-fitting σ to be consistent with 0 at a 2σ level. However, ELG and QSO samples constrain σ weakly. Although the loose constraint from the QSO sample is mostly due to its small number density, this does not stand for ELGs which are over 10 times denser than QSOs. We attribute this lack of constraint to the fact that σ also models the incompleteness in both stellar mass and luminosity, resulting in a complex galaxy–halo relation that is harder to constrain.

$V_{\rm ceil}$, the massive-(sub)halo incompleteness, describes the stellar mass incompleteness in the massive end due to both target selection criteria of galaxy surveys and the intrinsic properties of certain galaxies. The best-fitting $V_{\rm ceil}$ for LRGs, is as small as 0.02 per cent. This small value shows that DESI LRGs from the One Percent Survey are close to complete at the massive end. The best-fitting $V_{\rm ceil}$ for ELGs shows that up to 7 per cent of (sub)haloes that have the largest $V_{\rm scat}$ (equation 13) in the UNIT simulation would not host ELGs. Although QSOs are the brightest object at $z > 1$, their best-fitting $V_{\rm ceil}$ is inconsistent with zero, suggesting that not all haloes above a certain mass will be hosting a QSO. Their absence in the centre of massive (sub)haloes is consistent with the depletion of cold gas in this hot and dense environment there, leading to the quenching of ELG star formation and QSO black hole accretion. This agrees with the scenarios found in SAM studies and observations (e.g. Uchiyama et al. 2018; Griffin et al. 2019; Gonzalez-Perez et al. 2020).

$v_{\rm smear}$ quantifies the effect that the redshift uncertainty has on the clustering. It can also be measured statistically and independently by the redshift difference Δv of repeat observations (see Section 2.2). The Δv histogram of DESI tracers follows, in general, a Lorentzian profile with width $w_{\Delta v}$, instead of a single Gaussian profile as was found for BOSS/eBOSS galaxies. Thus, we have developed SHAM algorithms with a truncated Lorentzian profile for modelling the redshift uncertainty, that is, $v_{\rm smear,\,L}$. The Δv of LRG subsamples in different redshift bins can be fitted well by a Lorentzian or a Gaussian profile and thus, we also develop a Gaussian $v_{\rm smear,\,G}$ for LRGs. The Lorentzian $v_{\rm smear,\,L}$ of LRGs is only consistent with $w_{\Delta v}$ at $0.4 < z < 1.1$. The clustering of LRG sub-samples in redshift bins actually suggests a preference for a Gaussian profile for the redshift uncertainty. Nevertheless, truncated Lorentzian and Gaussian functions provide the same SHAM clustering and consistent best-fitting σ and $V_{\rm ceil}$. For QSOs, $v_{\rm smear,\,L}$ monotonically increases and deviates from $w_{\Delta v}$ at $z > 1.5$. This is because the C IV line used to determine QSO redshifts is affected by the velocity shifts of spectral lines that can vary between objects. Although the repeat observation cannot capture this feature, its effect on the clustering will be modelled by SHAM $v_{\rm smear,\,L}$. This is consistent with the eBOSS QSO analysis (Zarrouk et al. 2018).

The satellite fraction $f_{\rm sat}$ of LRG and QSO samples is fixed to the number of subhaloes from the UNIT simulation included for the SHAM, given σ and $V_{\rm ceil}$. Their $f_{\rm sat}$ decreases with redshift, following the evolution of the subhalo fraction in the simulations. For ELGs, we use the $f_{\rm sat}$-SHAM, setting $f_{\rm sat}$ as a free parameter. The best-fitting $f_{\rm sat}$ for DESI ELGs is around 4 per cent. This low value is consistent with previous studies for strong [O II] emitters (Gonzalez-Perez et al. 2020; Gao et al. 2022), but it is lower than the estimations for the total ELG samples (Favole et al. 2016; Guo et al. 2019; Lin et al. 2023).

We provide the HOD measured from our best-fitting SHAM for LRGs, ELGs, and QSOs from the One Percent Survey. The HOD of SHAM central LRGs reaches its peak at $\langle N\rangle = 0.75 \pm 0.07$ and is consistent with an incomplete LRG pattern as found in Yuan et al. 2023a. The HOD for central SHAM ELGs is consistent with a star-forming HOD profile peaking at $\langle N_{\rm cen}\rangle = 0.06 \pm 0.03$ and $M_{\rm vir} = 10^{11.7}\,h^{-1}\,{\rm M}_{\odot}$, but we cannot exclude a Gaussian shape (e.g., Avila et al. 2020). The HOD for SHAM central QSO also decreases after $M_{\rm vir} = 10^{12.4}\,h^{-1}\,{\rm M}_{\odot}$ with $\langle N\rangle = 0.016 \pm 0.001$. The HOD for all types of SHAM satellite galaxies is composed of two exponential functions with different slopes. The slope α in the massive halo end is $\alpha_{\rm LRG} = 0.70^{+0.01}_{-0.01}$, $\alpha_{\rm ELG} = 0.76^{+0.06}_{-0.07}$, and $\alpha_{\rm QSO} = 0.73^{+0.07}_{-0.07}$. They

Downloaded from https://academic.oup.com/mnras/article/527/3/6950/7438901 by University College London user on 06 February 2024

are smaller than the measurements from ABACUSSUMMIT HOD tests for LRGs but consistent with those from ELGs and QSOs (Rocher et al. 2023; Yuan et al. 2023a). We shall point out that the decreasing halo occupation of centrals with respect to the halo mass for LRGs, ELGs, and QSOs is a result of the simple $V_{\rm scat}$ truncation, that is, the implementation of $V_{\rm ceil}$. Galaxy clustering produced by this profile is consistent with that from HOD models with other profiles. So we need more data with higher accuracy and physical models in SHAM/HOD to give a better description of this halo occupation incompleteness on the massive end. The cross-validation of the halo occupation number among hydrodynamical simulations, SAM, forward modelling, SHAM and HOD is planned for future work. This is because we have yet a consistent clustering measurement with the observation for all methods and the series of mock galaxies generated by those methods on the same simulation.

We measure a mean parent halo mass of $\langle M_{\rm vir}\rangle = 10^{13.16\pm0.01}\,h^{-1}\,{\rm M}_\odot$ for LRGs, $10^{11.90\pm0.06}\,h^{-1}\,{\rm M}_\odot$ for ELGs, and $10^{12.66\pm0.45}\,h^{-1}\,{\rm M}_\odot$ for QSOs. For subsamples at redshift bins, we obtain $\langle M_{\rm vir}\rangle$ that decreases with redshift for LRGs and QSOs, but not for ELGs. Meanwhile, the linear bias for each tracer increases with the redshift. Those results are consistent with the HOD measurement using the same tracers from the One Percent Survey in general.

We also provide the SHAM-calibrated probability distribution of $V_{\rm peak}$ for LRGs, ELGs, and QSOs at $0.8 < z < 1.1$. LRGs and QSOs are populated in (sub)haloes with a similar range of $V_{\rm peak}$, $\langle V_{\rm peak,LRG}\rangle = 457 \pm 6\,{\rm km\,s^{-1}}$ and $\langle V_{\rm peak,QSO}\rangle = 346 \pm 8\,{\rm km\,s^{-1}}$. The value for ELG (sub)haloes is smaller, $\langle V_{\rm peak,ELG}\rangle = 159 \pm 4\,{\rm km\,s^{-1}}$. This result will be useful for future multitracer studies.

SHAM algorithms that include the redshift uncertainty, massive-(sub)halo incompleteness and an adjustable satellite fraction work well in the single-tracer case, which can provide galaxy mocks for cosmological tests (e.g. Su et al. 2023). We plan to enhance this study in the future by implementing a multitracer SHAM method based on what we have learned from this study.

ACKNOWLEDGEMENTS

JY, CZ, and JPK acknowledge support from the SNF 200020_175751 and 200020_207379 'Cosmology with 3D Maps of the Universe' research grant. VGP is supported by the Atracción de Talento contract no. 2019-T1/TIC-12702 granted by the Comunidad de Madrid in Spain and by the Ministerio de Ciencia e Innovación (MICINN) under research grant PID2021-122603NB-C21. We would like to thank Risa Wechsler, Christophe Yèche, Zheng Zheng, Charling Tao, Philip Mansfield, Hong Guo, Jeffrey Newman, Cheng Li, Haowen Zhang, Xiangyu Jin, Xi Kang, and Svyatoslav Trusov for their helpful discussions. We also thank John Helly for providing us with the Millennium simulation.

This material is based upon work supported by the U.S. Department of Energy (DOE), Office of Science, Office of High-Energy Physics, under contract no. DE–AC02–05CH11231, and by the National Energy Research Scientific Computing Center, a DOE Office of Science User Facility under the same contract. Additional support for DESI was provided by the U.S. National Science Foundation (NSF), Division of Astronomical Sciences under contract no. AST-0950945 to the NSF's National Optical-Infrared Astronomy Research Laboratory; the Science and Technology Facilities Council of the United Kingdom; the Gordon and Betty Moore Foundation; the Heising-Simons Foundation; the French Alternative Energies and Atomic Energy Commission (CEA); the National Council of Science and Technology of Mexico (CONACYT); the Ministry of Science and Innovation of Spain (MICINN), and by the DESI Member Institutions: https://www.desi.lbl.gov/collaborating-institutions. Any opinions, findings, and conclusions or recommendations expressed in this material are those of the author(s) and do not necessarily reflect the views of the U. S. National Science Foundation, the U. S. Department of Energy, or any of the listed funding agencies.

The authors are honoured to be permitted to conduct scientific research on Iolkam Du'ag (Kitt Peak), a mountain with particular significance to the Tohono O'odham Nation.

DATA AVAILABILITY

All the figures and the best-fitting mock galaxies of SHAM are available in Zenodo: https://doi.org/10.5281/zenodo.7889632.

REFERENCES

Alam S. et al., 2021a, Phys. Rev. D, 103, 083533
Alam S. et al., 2021b, MNRAS, 504, 4667
Alam S., Peacock J. A., Kraljic K., Ross A. J., Comparat J., 2020, MNRAS, 497, 581
Alexander D. M. et al., 2023, AJ, 165, 124
Allende Prieto C. et al., 2020, Res. Notes Am. Astron. Soc., 4, 188
Angulo R. E., Pontzen A., 2016, MNRAS, 462, L1
Avila S. et al., 2020, MNRAS, 499, 5486
Bautista J. E. et al., 2021, MNRAS, 500, 736
Behroozi P. S., Conroy C., Wechsler R. H., 2010, ApJ, 717, 379
Behroozi P. S., Wechsler R. H., Wu H.-Y., 2013a, ApJ, 762, 109
Behroozi P. S., Wechsler R. H., Wu H.-Y., Busha M. T., Klypin A. A., Primack J. R., 2013b, ApJ, 763, 18
Behroozi P., Wechsler R. H., Hearin A. P., Conroy C., 2019, MNRAS, 488, 3143
Bianchi D., Percival W. J., 2017, MNRAS, 472, 1106
Blanton M. R. et al., 2017, AJ, 154, 28
Buchner J. et al., 2014, A&A, 564, A125
Campbell D., van den Bosch F. C., Padmanabhan N., Mao Y.-Y., Zentner A. R., Lange J. U., Jiang F., Villarreal A. S., 2018, MNRAS, 477, 359
Chaussidon E. et al., 2023, ApJ, 944, 107
Chuang C.-H. et al., 2019, MNRAS, 487, 48
Conroy C., Wechsler R. H., Kravtsov A. V., 2006, ApJ, 647, 201
Contreras S., Angulo R. E., Zennaro M., 2021a, MNRAS, 504, 5205
Contreras S., Angulo R. E., Zennaro M., 2021b, MNRAS, 508, 175
Cooper A. P. et al., 2023, ApJ, 947, 37
Dawson K. S. et al., 2012, AJ, 145, 10
Dawson K. S. et al., 2016, AJ, 151, 44
Dekel A., Birnboim Y., 2006, MNRAS, 368, 2
DeRose J., Becker M. R., Wechsler R. H., 2022, ApJ, 940, 13
DESI Collaboration, 2016a, preprint (arXiv:1611.00036)
DESI Collaboration, 2016b, preprint (arXiv:1611.00037)
DESI Collaboration, 2022, AJ, 164, 207
DESI Collaboration, 2023a, preprint (arXiv:2306.06307)
DESI Collaboration, 2023b, preprint (arXiv:2306.06308)
Dey A. et al., 2019, AJ, 157, 168
Eisenstein D. J. et al., 2011, AJ, 142, 72
Eisenstein D. J., Hu W., 1998, ApJ, 496, 605
Favole G. et al., 2016, MNRAS, 461, 3421
Favole G., Montero-Dorta A. D., Artale M. C., Contreras S., Zehavi I., Xu X., 2022, MNRAS, 509, 1614
Feldman H. A., Kaiser N., Peacock J. A., 1994, ApJ, 426, 23
Feroz F., Hobson M. P., 2008, MNRAS, 384, 449
Feroz F., Hobson M. P., Bridges M., 2009, MNRAS, 398, 1601
Feroz F., Hobson M. P., Cameron E., Pettitt A. N., 2019, OJAp, 2, 10
Gao H. et al., 2023, ApJ, 954, 207
Gao H., Jing Y. P., Zheng Y., Xu K., 2022, ApJ, 928, 10
Gaskell C. M., 1982, ApJ, 263, 79
Gonzalez-Perez V. et al., 2018, MNRAS, 474, 4024

Downloaded from https://academic.oup.com/mnras/article/527/3/6950/7438901 by University College London user on 06 February 2024

Gonzalez-Perez V. et al., 2020, MNRAS, 498, 1852
Gonzalez-Perez V., Lacey C. G., Baugh C. M., Lagos C. D. P., Helly J., Campbell D. J. R., Mitchell P. D., 2014, MNRAS, 439, 264
Griffin A. J., Lacey C. G., Gonzalez-Perez V., Lagos C. d. P., Baugh C. M., Fanidakis N., 2019, MNRAS, 487, 198
Guo H. et al., 2015, MNRAS, 453, 4368
Guo H. et al., 2019, ApJ, 871, 147
Guy J. et al., 2023, AJ, 165, 144
Hadzhiyska B., Tacchella S., Bose S., Eisenstein D. J., 2021, MNRAS, 502, 3599
Hahn C. et al., 2023, AJ, 165, 253
Hartlap J., Simon P., Schneider P., 2007, A&A, 464, 399
Hearin A. P., Zentner A. R., Berlind A. A., Newman J. A., 2013, MNRAS, 433, 659
Hou J. et al., 2018, MNRAS, 480, 2521
Ishiyama T. et al., 2021, MNRAS, 506, 4210
Jing Y., 2019, Sci. China Phys. Mech. Astron., 62, 19511
Kaiser N., 1987, MNRAS, 227, 1
Kauffmann G., White S. D. M., Heckman T. M., Ménard B., Brinchmann J., Charlot S., Tremonti C., Brinkmann J., 2004, MNRAS, 353, 713
Kitaura F.-S. et al., 2016, MNRAS, 456, 4156
Kravtsov A. V., Berlind A. A., Wechsler R. H., Klypin A. A., Gottlober S., Allgood B., Primack J. R., 2004, ApJ, 609, 35
Lan T.-W. et al., 2023, ApJ, 943, 68
Landy S. D., Szalay A. S., 1993, ApJ, 412, 64
Leauthaud A. et al., 2012, ApJ, 744, 159
Lehmann B. V., Mao Y.-Y., Becker M. R., Skillman S. W., Wechsler R. H., 2017, ApJ, 834, 37
Levi M. et al., 2013, preprint (arXiv:1308.0847)
Lewis A., 2019, preprint (arXiv:1910.13970)
Lin S., Tinker J. L., Blanton M. R., Guo H., Raichoor A., Comparat J., Brownstein J. R., 2023, MNRAS, 519, 4253
Lyke B. W. et al., 2020, ApJS, 250, 8
Maksimova N. A., Garrison L. H., Eisenstein D. J., Hadzhiyska B., Bose S., Satterthwaite T. P., 2021, MNRAS, 508, 4017
Miller T. N. et al., 2023, preprint (arXiv:2306.06310)
Mohammad F. G. et al., 2020, MNRAS, 498, 128
Myers A. D. et al., 2023, AJ, 165, 50
Parejko J. K. et al., 2013, MNRAS, 429, 98
Pearl A. N. et al., 2023, preprint (arXiv:2309.08675)
Peebles P. J. E., Hauser M. G., 1974, ApJS, 28, 19
Peng Y.-j. et al., 2010, ApJ, 721, 193
Percival W. J., Bianchi D., 2017, MNRAS, 472, L40
Planck Collaboration XIII, 2016, A&A, 594, A13
Prada F. et al., 2023, preprint (arXiv:2306.06315)
Prada F., Klypin A. A., Cuesta A. J., Betancort-Rijo J. E., Primack J., 2012, MNRAS, 423, 3018
Raichoor A. et al., 2020, Res. Notes Am. Astron. Soc, 4, 180
Raichoor A. et al., 2023, AJ, 165, 126
Reddick R. M., Wechsler R. H., Tinker J. L., Behroozi P. S., 2013, ApJ, 771, 30
Richards G. T. et al., 2011, AJ, 141, 167
Richards G. T., Vanden Berk D. E., Reichard T. A., Hall P. B., Schneider D. P., SubbaRao M., Thakar A. R., York D. G., 2002, AJ, 124, 1
Rocher A. et al., 2023, J. Cosmol. Astropart. Phys., 2023, 016
Rodríguez-Torres S. A. et al., 2016, MNRAS, 460, 1173
Rodríguez-Torres S. A. et al., 2017, MNRAS, 468, 728
Rosario D. J. et al., 2013, A&A, 560, A72
Ross A. J. et al., 2014, MNRAS, 437, 1109
Ross A. J. et al., 2017, MNRAS, 464, 1168
Ross A. J. et al., 2020, MNRAS, 498, 2354
Ruiz-Macias O. et al., 2020, Res. Notes Am. Astron. Soc., 4, 187
Schlafly E. F. et al., 2023, preprint (arXiv:2306.06309)
Scodeggio, 2018, A&A, A84, 0004
Shen Y. et al., 2016, ApJ, 831, 7
Silber J. H. et al., 2022, AJ, 165, 9
Sinha M., Garrison L. H., 2020, MNRAS, 491, 3022
Sinha M., Garrison L., 2019, in Majumdar A., Arora R.eds, Software Challenges to Exascale Computing. Springer Singapore, Singapore, p. 3
Smith A. et al., 2020, MNRAS, 499, 269
Smith A., de Mattia A., Burtin E., Chuang C.-H., Zhao C., 2021, MNRAS, 500, 259
Springel V. et al., 2005, Nature, 435, 629
Steinmetz M., Navarro J., 1999, ApJ, 513, 555
Su C. et al., 2023, ApJ, 951, 64
Tasitsiomi A., Kravtsov A. V., Wechsler R. H., Primack J. R., 2004, ApJ, 614, 533
Tinker J., Wetzel A., Conroy C., 2011, preprint (arXiv:1107.5046)
Trujillo-Gomez S., Klypin A., Primack J., Romanowsky A. J., 2011, ApJ, 742, 16
Uchiyama H. et al., 2018, PASJ, 70, S32
van den Bosch F. C., Ogiya G., 2018, MNRAS, 475, 4066
van den Bosch F. C., Ogiya G., Hahn O., Burkert A., 2018, MNRAS, 474, 3043
Wang Y., Chuang C.-H., Hirata C. M., 2013, MNRAS, 430, 2446
Weinberger R. et al., 2018, MNRAS, 479, 4056
Wetzel A. R., Tinker J. L., Conroy C., 2012, MNRAS, 424, 232
Willick J. A., Courteau S., Faber S. M., Burstein D., Dekel A., Strauss M. A., 1997, ApJS, 109, 333
Yèche C. et al., 2020, Res. Notes Am. Astron. Soc., 4, 179
Yu J. et al., 2022, MNRAS, 516, 57
Yuan S. et al., 2023a, preprint (arXiv:2306.06314)
Yuan S. et al., 2023b, preprint (arXiv:2310.09329)
Zarrouk P. et al., 2018, MNRAS, 477, 1639
Zhai Z. et al., 2017, ApJ, 848, 76
Zhao C. et al., 2021, MNRAS, 503, 1149
Zheng Z. et al., 2005, ApJ, 633, 791
Zhou R. et al., 2020, Res. Notes Am. Astron. Soc., 4, 181
Zhou R. et al., 2023, AJ, 165, 58
Zou H. et al., 2017, PASP, 129, 064101

APPENDIX A: 4-PARAMETER SHAM

SHAM with four parameters $\{\sigma, V_{\rm ceil}, v_{\rm smear}, f_{\rm sat}\}$ is the inclusive version of $v_{\rm smear}$-SHAM and $f_{\rm sat}$-SHAM. Fig. A1 provides the impact of those four parameters on the 2PCF monopole, quadrupole and projected 2PCF of UNIT-SHAM galaxies in the fitting range 5–30 h^{-1} Mpc. The 'standard' clustering is obtained from σ, $V_{\rm ceil}$, $v_{\rm smear} = 0$ using $v_{\rm smear}$-SHAM. So its $f_{\rm sat}$ is derived from its SHAM catalogue. When we have a larger σ as shown in the first column of Fig. A1, ξ_0 and w_p decrease systematically and ξ_2 rotates counterclockwise with respect to a point at $s \sim 6\,h^{-1}$ Mpc. A larger $V_{\rm ceil}$ leads to a similar effect as shown in the second column, with the rotating point moving to $s \sim 7\,h^{-1}$ Mpc in ξ_2. This is because both σ and $V_{\rm ceil}$ control the mass range of (sub)haloes that can host model galaxies given a fixed $N_{\rm gal}$.

$v_{\rm smear}$ and $f_{\rm sat}$ are another pair of parameters that can change the velocity distribution along the line of sight, thus degenerated with each other. As presented in the third column of Fig. A1, increasing $v_{\rm smear}$ causes a larger ξ_2 on 5–30 h^{-1} Mpc. A Gaussian $v_{\rm smear,\,G}$ does not have a huge impact on ξ_0 and w_p, while a Lorentzian profile $v_{\rm smear,\,L}$ with a truncation in 2000 km s^{-1} does influence ξ_0. Note that the clustering effect of a Lorentzian profile can be similar to that of a Gaussian profile as shown in Section 4.4. The difference in the clustering effect here should be attributed to both the $v_{\rm smear}$ value and truncation value. None the less, those two symmetric $v_{\rm smear}$ profiles can only lead to an increasing ξ_2 at 5–30 h^{-1} Mpc for SHAM galaxies compared to that of the 'standard' sample. In contrast, we can decrease ξ_2 with respect to the 'standard' one at similar scales by decreasing $f_{\rm sat}$. Note that those are the critical scales to reproduce the clustering of DESI ELG. Varying $f_{\rm sat}$ results in a systematical shift

Downloaded from https://academic.oup.com/mnras/article/527/3/6950/7438901 by University College London user on 06 February 2024

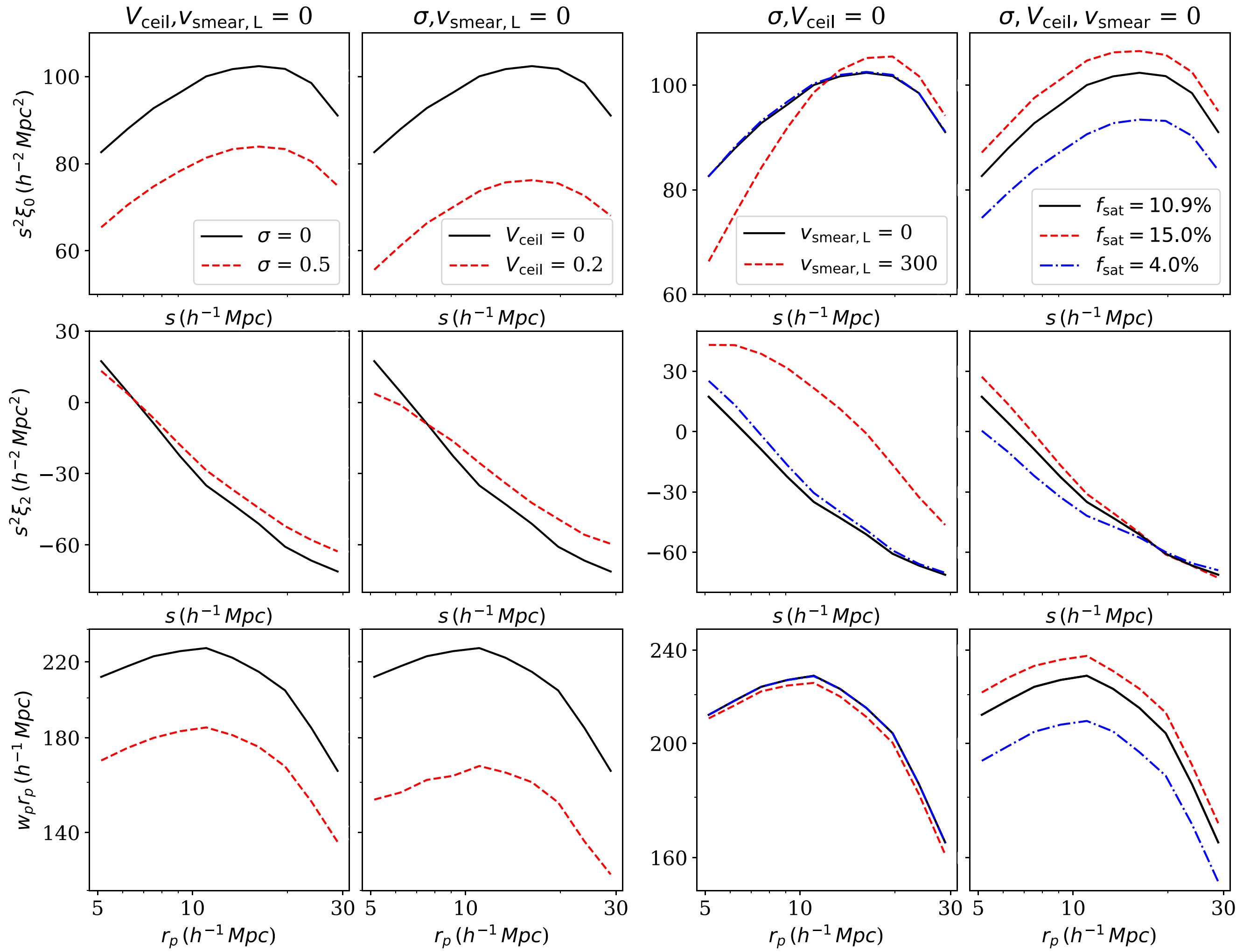

Figure A1. The impact of σ (first column), $V_{\rm ceil}$ (second column), $v_{\rm smear}$ (third column), and $f_{\rm sat}$ (fourth column) on the 2PCF monopole (first row), quadrupole (second row), and the projected 2PCF (third row). The standard sample is σ, $V_{\rm ceil}$, $v_{\rm smear} = 0$ with $f_{\rm sat} = 10.9$ per cent in solid lines. The first three columns show the 2PCF difference between the standard sample and samples with $\sigma = 0.5$, $V_{\rm ceil} = 0.2$ per cent or $v_{\rm smear,L} = 300\,{\rm km\,s^{-1}}$ (truncated at $2000\,{\rm km\,s^{-1}}$), respectively, while fixing the other two parameters, in dashed lines. Results of $v_{\rm smear}$-SHAM with a Gaussian profile $v_{\rm smear,G} = 80\,{\rm km\,s^{-1}}$ are also presented in the third column in dashdotted lines. In the last column, we compare the 2PCF for SHAM galaxies with $f_{\rm sat} = 15$ per cent (dashed lines) and $f_{\rm sat} = 4$ per cent (dashdotted lines) with that of the standard sample in $f_{\rm sat}$-SHAM with σ, $V_{\rm ceil}$, $v_{\rm smear} = 0$ (solid lines).

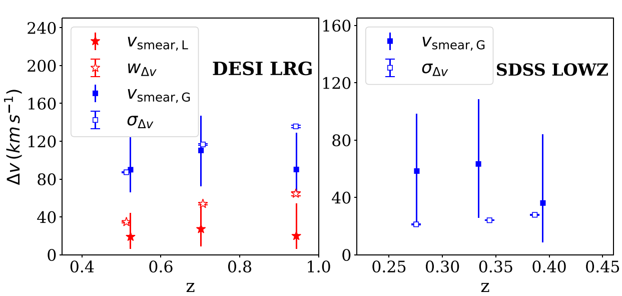

Figure A2. The redshift uncertainty measured from repeat observation (filled error bars) and from SHAM (empty error bars) for 4-parameter SHAM for LRGs (left panel) and SDSS-III LOWZ (right panel). Results for Lorentzian profiles are presented in star markers and those of Gaussian profiles are in square markers. Note that the Gaussian measurements for DESI LRGs are shifted by $40\,{\rm km\,s^{-1}}$ upwards.

for ξ_0 and w_p as well.

We apply the 4-parameter SHAM to LRGs from the One Percent Survey for a consistency check with $v_{\rm smear}$ SHAM. We also perform a SHAM test for SDSS-III BOSS LOWZ samples, trying to resolve the overestimation of redshift uncertainty by $v_{\rm smear}$-SHAM found in Yu22. In Fig. A2, we present the $v_{\rm smear}$ from the best-fitting 4-parameter SHAM together with $w_{\Delta v}$ and $\sigma_{\Delta v}$ from the repeat observations for DESI LRGs (left) and LOWZ LRG samples (right). Comparing with Fig. 6, $v_{\rm smear}$ values systematically shift to smaller values. The satellite fraction of 4-parameter SHAM is consistent with that of $v_{\rm smear}$-SHAM, except for LRGs at $0.8 < z < 1.1$ with Gaussian profile, for which the $v_{\rm smear,\,G}$ result becomes inconsistent with $\sigma_{\Delta v}$ of repeat observations. As we have a reliable statistical measurement of LRG redshift uncertainty, it means that the satellite fraction estimation might be biased by the redshift uncertainty.

For the LOWZ 4-parameter SHAM study, the basic information of LOWZ observation, including UNIT simulations and the best-fitting SHAM results is presented in Table A1. Our best-fitting $v_{\rm smear}$

Downloaded from https://academic.oup.com/mnras/article/527/3/6950/7438901 by University College London user on 06 February 2024

Table A1. The same as Table 2, but for 4-parameter SHAM with $\{\sigma, V_{\rm ceil}, v_{\rm smear}, f_{\rm sat}\}$ applied on BOSS LOWZ clustering at $0.2 < z < 0.43$.

Redshift range	$z_{\rm eff}$	$z_{\rm UNIT}$	$V_{\rm eff}$ (h^{-3} Gpc^3)	$10^4 n_{\rm eff}$ (h^3 Mpc^{-3})	σ	$v_{\rm smear,\,G}$ (km s^{-1})	$V_{\rm ceil}$ (per cent)	$f_{\rm sat}$ (per cent)	χ^2/d.o.f.
$0.2 < z < 0.43$	0.3441	0.3337	0.62	2.95	$0.19^{+0.06}_{-0.06}$	63^{+45}_{-37}	$0.0045^{+0.0048}_{-0.0030}$	$13.55^{+2.07}_{-3.13}$	51/37
$0.2 < z < 0.33$	0.2754	0.2760	0.29	3.37	$0.15^{+0.09}_{-0.10}$	58^{+40}_{-38}	$0.0077^{+0.0060}_{-0.0048}$	$15.87^{+1.81}_{-3.11}$	32/37
$0.33 < z < 0.43$	0.3865	0.3941	0.33	2.58	$0.27^{+0.05}_{-0.07}$	36^{+48}_{-28}	$0.0030^{+0.0038}_{-0.0021}$	$13.48^{+1.13}_{-2.66}$	50/37

are consistent with $\sigma_{\Delta v}$, resolving the discrepancy shown in Fig. 6 of Yu22. The $v_{\rm smear}$–$f_{\rm sat}$ degeneracy enables $v_{\rm smear}$ to decrease to the observed uncertainty level by increasing its satellite fraction. Meanwhile, our best-fitting $f_{\rm sat}$ is consistent with the LOWZ HOD $f_{\rm sat} = 12 \pm 2$ per cent (Parejko et al. 2013).

APPENDIX B: POSTERIOR CONTOURS

In Figs B1–B4, we present the posteriors of the fittings from Table 2, that is, those of $v_{\rm smear}$-SHAM for LRG samples and QSOs, and $f_{\rm sat}$-SHAM for ELG samples. The $v_{\rm smear}$ profile here is Lorentzian. They are plotted using GETDIST (Lewis 2019). All fittings have converged and are ended by the nested sampling automatically.

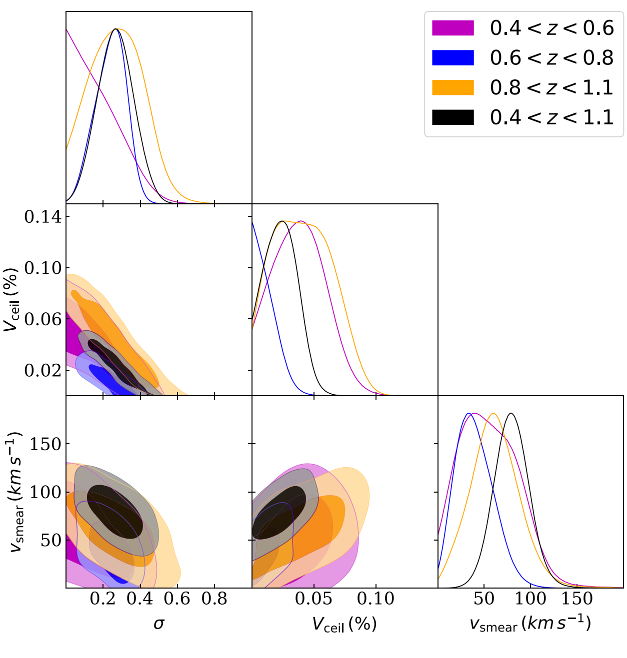

Figure B1. The posterior corner plot for LRGs at $0.4 < z < 0.6$, $0.6 < z < 0.8$, $0.8 < z < 1.1$, and $0.4 < z < 1.1$. The parameters are σ, $V_{\rm ceil}$, and $v_{\rm smear}$.

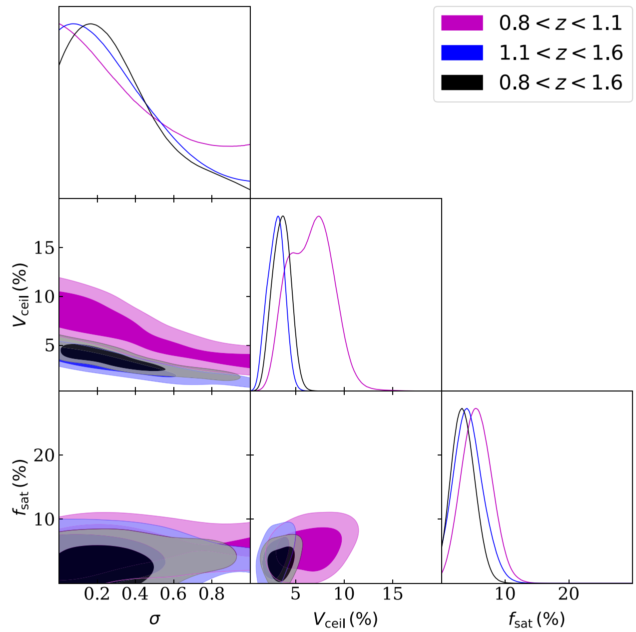

Figure B2. The posterior corner plot for ELGs at $0.8 < z < 1.1$, $1.1 < z < 1.6$, and $0.8 < z < 1.6$. The parameters are σ, $V_{\rm ceil}$, and $f_{\rm sat}$.

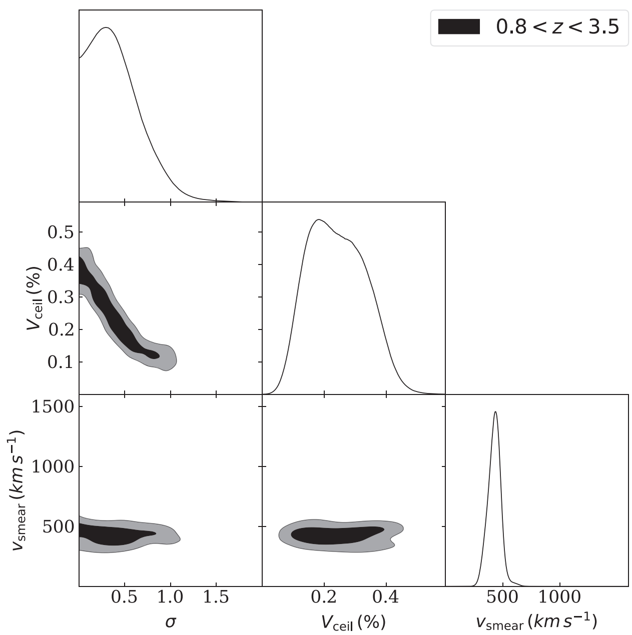

Figure B3. The same as Fig. B1, but for QSOs at $0.8 < z < 3.5$.

Downloaded from https://academic.oup.com/mnras/article/527/3/6950/7438901 by University College London user on 06 February 2024

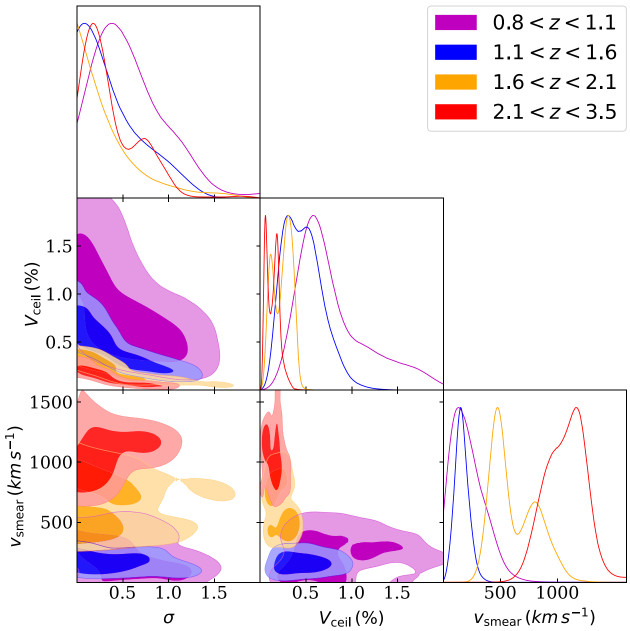

Figure B4. The same as Fig. B1, but for QSOs at $0.8 < z < 1.1$, $1.1 < z < 1.6$, $1.6 < z < 2.1$, and $2.1 < z < 3.5$.

APPENDIX C: REPRODUCED w_p

We provide the comparison between mock galaxies of SHAM and observations for the projected 2PCF $w_p r_p$ at 5–30 h^{-1} Mpc in Figs C1–C3. The mock galaxies are constructed using the parameter set of SHAM that corresponds to the minimum χ^2. The $\pi_{\rm max}$ of their w_p are 30 h^{-1} Mpc (Section 3.1). The best-fitting reduced χ^2 of LRG at $0.8 < z < 1.1$ is larger than 1.5, but the reproduced w_p agrees with the observation. So mock galaxies of SHAM for this sample are still a good description of the observed clustering.

We note the disagreement on scales smaller than 1 h^{-1} Mpc between the observation and the prediction of the best-fitting SHAM galaxy mocks in general as illustrated in Fig. C4. This is probably due to the overdisruption or overmerging of subhaloes in *N*-body

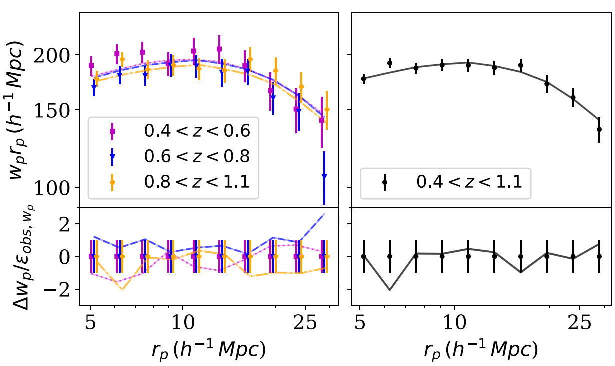

Figure C1. The projected 2PCFs $w_p r_p$ of observed LRGs (filled error bars) and those of the best-fitting SHAM galaxies (lines with shades) with $\pi_{\rm max} = 30\,h^{-1}$ Mpc. The direct comparison and residuals rescaled by the observed error bars are presented in the first and the second rows, respectively. *The left panel:* the squared, down-triangle, and filled plus markers are observed LRGs at $0.4 < z < 0.6$, $0.6 < z < 0.8$, $0.8 < z < 1.1$ with slight horizontal shift and the dotted, dashed, dashdot lines corresponds to their best-fit SHAM clustering with the same shift. *The right panel*: the total sample results at $0.4 < z < 1.1$.

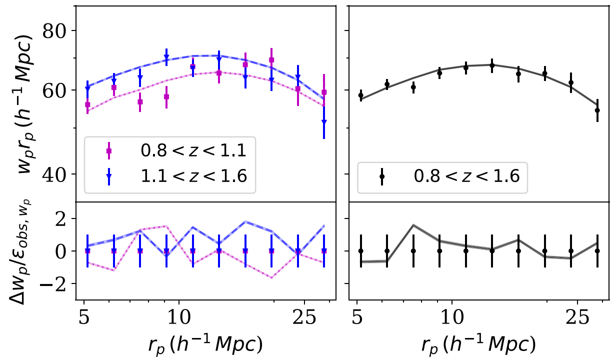

Figure C2. Same as Fig. C1, but for ELGs.

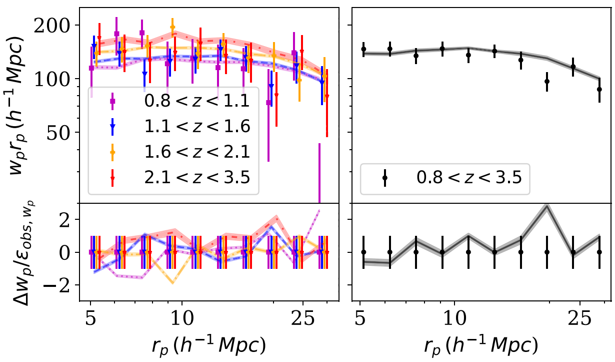

Figure C3. Same as Fig. C1, but for QSOs.

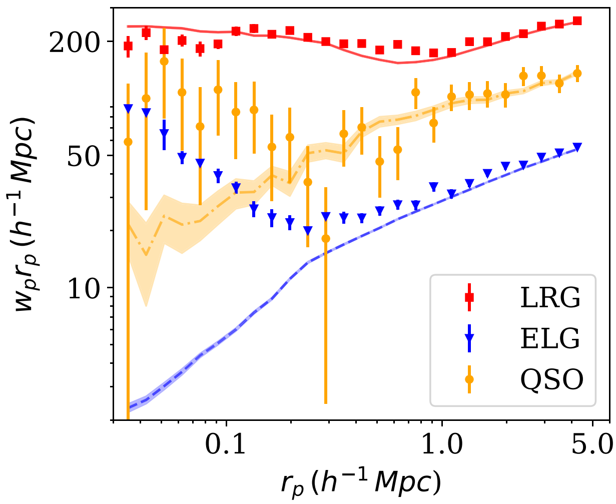

Figure C4. The projected 2PCF $w_p r_p$ at 0.01–5 h^{-1} Mpc of observations (filled error bars) and the predictions from the best-fitting SHAM (lines with shades). LRGs are represented by squared error bars and the solid line, ELGs are triangle error bars and the dashed line, QSOs are circle error bars and the dashdotted line. The $w_p r_p$ of LRGs is vertically shifted.

Downloaded from https://academic.oup.com/mnras/article/527/3/6950/7438901 by University College London user on 06 February 2024

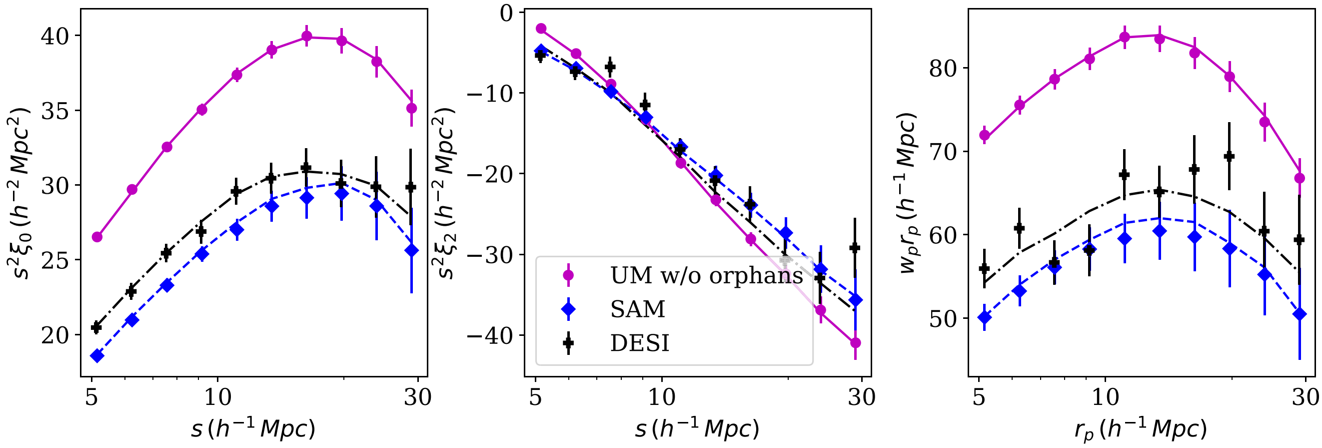

Figure C5. The 2PCF of UniverseMachine ELGs (circles error bars) at $z = 0.9436$, SAM ELGs (diamond error bars) at $z = 0.99$, and DESI ELGs (filled plus error bars) with $z_{\rm eff} = 0.9565$, and their corresponding best-fitting SHAM galaxies in dashed, solid and dashdotted lines respectively. The 2PCF monopoles, quadrupole, and projected 2PCF are presented in the left, middle, and right panels.

simulations (e.g. van den Bosch & Ogiya 2018; van den Bosch et al. 2018; Behroozi et al. 2019). In addition to that, the uprising small-scale $w_p r_p$ of DESI ELGs may have physical explanations as shown in Rocher et al. (2023).

APPENDIX D: IS SATELLITE FRACTION BIASED?

To validate our satellite fraction in $f_{\rm sat}$-SHAM measurement, we use other galaxy mocks as observations. They are constructed in various galaxy–halo models and have the same definition of satellites as our SHAM, that is, galaxies residing in subhaloes. By implementing $f_{\rm sat}$-SHAM on the same N-body simulations as those model galaxies and fitting the 2PCF monopole and quadrupole of those modelled galaxies on 5–30 h^{-1} Mpc, $f_{\rm sat}$ of the best-fitting SHAM is expected to be consistent with the true value of those galaxy mocks. The covariance matrices we used here are calculated with jackknife subsamples of other mock galaxies produced by PYCORR.

The first set of galaxies is from a DESI-like ELG catalogue established with SAM (Gonzalez-Perez et al. 2014, 2020, SAM ELG hereafter) at redshift $z = 0.99$ with $f_{\rm sat} = 4.14$ per cent. The corresponding N-body simulation is MILLENNIUM[9] with the Wilkinson Microwave Anisotropy Probe-7 (WMAP7) cosmology (Springel et al. 2005). As there is no $V_{\rm peak}$ in this simulation, we use $V_{\rm max}$ for $f_{\rm sat}$-SHAM. Another sample of star-forming galaxies from UniverseMachine (Behroozi et al. 2019, UniverseMachine ELG hereafter) at $z = 0.9436$ with star formation rate larger than $10^{1.1}\,{\rm M}_{\odot}{\rm yr}^{-1}$ and $10^{9.6} < M_* < 10^{11}\,{\rm M}_{\odot}$. This galaxy catalogue is based on the snapshot of MULTIDARK MDPL2 simulation (Prada et al. 2012) at the same redshift[10] Orphan galaxies (Campbell et al. 2018; Behroozi et al. 2019) are removed from this sample to ensure a fair comparison to our SHAM-reproduced results as MULTIDARK simulations do not include this reconstruction on subhaloes by default. Finally, the star-forming galaxies from UniverseMachine are downsampled to have $n_{\rm gal} = 10.28 \times 10^{-4}\,{\rm Mpc}^{-3}h^3$, 1.8 per cent smaller than that of DESI ELGs at $0.8 < z < 1.1$.

Fig. C5 shows the clustering of SAM ELGs (diamond error bars), UniverseMachine ELGs (circle error bars), and DESI ELGs (filled plus error bars), and the clustering of the best-fitting SHAM galaxies (dashed lines for SAM, solid lines for UniverseMachine and dashdotted lines for DESI). Our $f_{\rm sat}$-SHAM can describe the 2PCF multipoles for SAM ELGs and UniverseMachine ELGs and reproduce their projected 2PCF on 5–30 h^{-1} Mpc. The best-fitting $f_{\rm sat}$ for SAM ELGs is $11.5^{+1.46}_{-1.19}$ per cent, which is a 6σ overstimation. Meanwhile, that for UniverseMachine ELGs is $12.60^{+0.76}_{-0.82}$ per cent, consistent with the true value. The inconsistency in the estimation of the satellite fraction among different galaxy–halo models needs further discussion in future studies.

[9] https://virgodb.dur.ac.uk:8443/Millennium/Help?page=databases/gonzalez2014a/mr7
[10] https://www.cosmosim.org/metadata/mdpl2/

[1] *Laboratory of Astrophysics, École Polytechnique Fédérale de Lausanne (EPFL), Observatoire de Sauverny, CH-1290 Versoix, Switzerland*
[2] *Department of Astronomy, Tsinghua University, Beijing 100084, China*
[3] *Departamento de Física Teórica, Facultad de Ciencias, Universidad Autónoma de Madrid, E-28049 Madrid, Spain*
[4] *Centro de Investigación Avanzada en Física Fundamental (CIAFF), Facultad de Ciencias, Universidad Autónoma de Madrid, E-28049 Madrid, Spain*
[5] *Department of Physics and Astronomy, University of Utah, Salt Lake City, UT 84112, USA*
[6] *IRFU, CEA, Université Paris-Saclay, F-91191 Gif-sur-Yvette, France*
[7] *LAM (Laboratoire d'Astrophysique de Marseille), Aix Marseille Université, CNRS, UMR 7326, F13388, Marseille, France*
[8] *Perimeter Institute for Theoretical Physics, 31 Caroline St. North, Waterloo, ON N2L 2Y5, Canada*
[9] *Waterloo Centre for Astrophysics, University of Waterloo, Waterloo, ON N2L 3G1, Canada*
[10] *Department of Physics and Astronomy, University of Waterloo, 200 University Avenue W, Waterloo, ON N2L 3G1, Canada*
[11] *Center for Cosmology and AstroParticle Physics, The Ohio State University, 191 West Woodruff Avenue, Columbus, OH 43210, USA*
[12] *Physics Department, Kavli Institute for Particle Astrophysics and Cosmology, Stanford University, Stanford, CA 94305, USA*
[13] *Physics Department, Stanford University, 382 Via Pueblo Mall, Stanford, CA 94305, USA*
[14] *SLAC National Accelerator Laboratory, Menlo Park, CA 94025, USA*
[15] *Department of Physics, Kansas State University, 116 Cardwell Hall, Manhattan, KS 66506, USA*
[16] *Lawrence Berkeley National Laboratory, 1 Cyclotron Road, Berkeley, CA 94720, USA*
[17] *Physics Department, Boston University, 590 Commonwealth Avenue, Boston, MA 02215, USA*

Downloaded from https://academic.oup.com/mnras/article/527/3/6950/7438901 by University College London user on 06 February 2024

[18]*Department of Physics & Astronomy, University College London, Gower Street, London, WC1E 6BT, UK*
[19]*Departamento de Física, Universidad de Guanajuato–DCI, C.P. 37150, Leon, Guanajuato, México*
[20]*Department of Physics, The Ohio State University, 191 West Woodruff Avenue, Columbus, OH 43210, USA*
[21]*Institut de Física d'Altes Energies(IFAE), The Barcelona Institute of Science and Technology, Campus UAB, E-08193 Bellaterra Barcelona, Spain*
[22]*Departamento de Física, Universidad de los Andes, Cra. 1 No. 18A-10, Edificio Ip, CP 111711, Bogotá, Colombia*
[23]*Department of Physics, Southern Methodist University, 3215 Daniel Avenue, Dallas, TX 75275, USA*
[24]*Serra Húnter Fellow, Departament de Física, Universitat Autònoma de Barcelona, 08193 Bellaterra (Barcelona), Spain*
[25]*Department of Astronomy, The Ohio State University, 140 W. 18th Ave., Columbus, OH 43210, USA*
[26]*NSF's National Optical-Infrared Astronomy Research Laboratory, 950 N. Cherry Avenue, Tucson, AZ 85719, USA*
[27]*Institució Catalana de Recerca i Estudis Avançats, Passeig de Lluís Companys, 23, E-08010 Barcelona, Spain*
[28]*Department of Physics and Astronomy, Siena College, 515 Loudon Road, Loudonville, NY 12211, USA*
[29]*National Astronomical Observatories, Chinese Academy of Sciences, A20 Datun Road, Chaoyang District, Beijing, 100101, People's Republic of China*
[30]*Space Sciences Laboratory, University of California, Berkeley, 7 Gauss Way, Berkeley, CA 94720, USA*
[31]*University of California, Berkeley, 110 Sproul Hall no. 5800 Berkeley, CA 94720, USA*
[32]*Department of Physics and Astronomy, Sejong University, Seoul 143-747, Korea*
[33]*Department of Physics and Astronomy, Ohio University, Athens, OH 45701, USA*
[34]*Department of Physics, University of Michigan, Ann Arbor, MI 48109, USA*

This paper has been typeset from a TEX/LATEX file prepared by the author.

Downloaded from https://academic.oup.com/mnras/article/527/3/6950/7438901 by University College London user on 06 February 2024

© 2023 The Author(s)
Published by Oxford University Press on behalf of Royal Astronomical Society. This is an Open Access article distributed under the terms of the Creative Commons Attribution License (https://creativecommons.org/licenses/by/4.0/), which permits unrestricted reuse, distribution, and reproduction in any medium, provided the original work is properly cited.